


Dissociative ionization of CO₂ in XUV pump and IR or visible probe pulsesVan-Hung Hoang  and Uwe Thumm *J. R. Macdonald Laboratory, Department of Physics, Kansas State University, Manhattan, Kansas 66506, USA* (Received 21 August 2023; revised 7 February 2024; accepted 8 March 2024; published 25 March 2024)

Following the sudden single ionization of CO₂ in ultrashort extreme ultraviolet pump pulses, after exposure to delayed 780- or 400-nm probe-laser pulses, we propagate the coupled nuclear motion in CO₂⁺ on the $A^2\Pi_u$, $B^2\Sigma_u^+$, $C^2\Sigma_g^+$, $a^4\Sigma_g^-$, and $b^4\Pi_u$ potential-energy surfaces of the excited molecular cation, including all vibronic degrees of freedom. We calculate potential-energy surfaces, diabatic couplings, and probe-laser-induced dipole couplings *ab initio* and heuristically model spin-orbit couplings. Based on our numerical results, we scrutinize the relative importance of diabatic, dipole, and spin-orbit couplings during the dissociation of CO₂⁺ into O(³P_g) + CO⁺($X^2\Sigma^+$) and O⁺(⁴S_u) + CO($X^1\Sigma^+$), provide rovibrational-excitation distributions of the CO⁺ fragments, and discuss pump-probe-delay-dependent kinetic-energy-release spectra. Addressing the nuclear dynamics near the conically intersecting $A^2\Pi_u$ and $B^2\Sigma_u^+$ states of CO₂⁺, we reproduce the valence-hole oscillation period of 115 fs measured by Timmers *et al.* [*Phys. Rev. Lett.* **113**, 113003 (2014)]. In addition, we predict and characterize, in terms of quantum beats between specific stationary vibronic states, a 3.1-ps fragment-yield oscillation.

DOI: [10.1103/PhysRevA.109.033117](https://doi.org/10.1103/PhysRevA.109.033117)**I. INTRODUCTION**

The forces exerted on molecular electrons by intense sources of electromagnetic radiation can be comparable to or outcompete intermolecular Coulomb interactions and thereby change the molecular electronic structure and dynamics. The strongly perturbed intramolecular electron dynamics can result in electronic excitation and ionization and typically affects the intramolecular nuclear motion. This leads to a variety of basic light-molecule-interaction phenomena, including nuclear configuration changes [1], dissociation [2–4], Coulomb explosion [5–8], bond softening and hardening [9–11], and valence-hole transfer [12]. Detecting, modeling, controlling, and understanding these dynamical processes in detail, i.e., at the timescale of the nuclear and electronic motion in molecules, is a key goal in ultrafast molecular physics and promotes our understanding of the intricate interplay between electronic and nuclear motion during chemical reactions. More specifically, these investigations promise to enable new efficient photocatalysis [13] and coherent-control schemes [14,15] for optimizing the desired outcome of chemical reactions and provide valuable insights for the synthesis of “designer” materials with desirable chemical and optical properties [16].

The most successful method for detecting the bound and dissociative dynamics in molecules is realized in pump-probe experiments [17–25]. Such experiments allow the resolution in time of the nuclear motion by first exciting and/or ionizing molecules in ultrashort pump pulses and then destructively imaging the excited nuclear dynamics in delayed ultrashort probe pulses. Scanning the preset delay τ between the intense pump and probe pulses over a sufficiently long time interval and detecting photoelectrons and/or molecular fragments as a function of τ , a stroboscopic sequence of electronic and/or fragment-momentum spectra can be recorded that resolves

the intramolecular dynamics at the natural timescales of the electronic (attoseconds [20]) or nuclear motion (femtoseconds [24,26]) in matter.

The initial nuclear motion produced by intense femtosecond (or shorter) pump pulses is frequently modeled in the Franck-Condon (FC) approximation as instantaneous excitation or ionization of the parent molecule [27,28]. This approximation represents the vibrational-state distribution of the excited or ionized molecule in terms of its wave-function overlap with the parent molecule, which is usually assumed in its electronic and vibronic ground state. The following coherent evolution of the excited cationic nuclear wave packet on a selected set of (adiabatic) Born-Oppenheimer (BO) potential-energy curves can, for small molecules, be traced in pump-probe experiments and numerically by solving the time-dependent Schrödinger equation (TDSE). This theoretical approach has been successfully compared with measured fragment kinetic-energy-release (KER) spectra for small molecules using ultrashort pump and probe pulses in different spectral domains. In particular, such pump-probe investigations have enabled the distinction of nuclear excitation and dissociation pathways in numerous experimental and theoretical studies with various diatomic molecules, for example, H₂ and D₂ [10,17–20,25,29–32], N₂ [7,21,22], O₂ [2,4,7,11,21,22,24,26,33], CO [7,21], and noble-gas dimers [23,34], using infrared (IR)–IR [7,17,19,21,29,33], extreme ultraviolet (XUV)–IR [20,24,26,31], vacuum ultraviolet–IR [32], XUV–XUV [4,22], and IR–soft-x-ray [35] pump-probe-pulse combinations.

We here extend our numerical modeling of dissociative ionization in XUV pump and IR or visible (VIS) probe pulses of diatomic molecules [2,10,11,18,23,34] to triatomic molecules [3,12,36–46]. Applying our model to the dissociative ionization of CO₂ by 18-eV central-photon-energy XUV pump pulses [12] and 780- or 400-nm probe-laser pulses,

we provide pump-probe-delay-dependent KER spectra, scrutinize two dissociation pathways, and discuss the imprint of a conical intersection on the nuclear dissociation dynamics and observable fragment yields. Our analysis of the CO_2^+ nuclear-wave-packet evolution reproduces the valence-hole oscillation period of 115 fs measured by Timmers *et al.* [12], reveals this period as a quantum beat between specific stationary vibronic states, and predicts a strong 3.1-ps oscillation contribution.

We organized this paper as follows. In Sec. II we review our numerical model for solving the TDSE, including all three nuclear degrees of freedom, in order to calculate fragment KER spectra. In Sec. III we discuss numerical results for the dissociative ionization of CO_2 , validating our calculation of relevant adiabatic potential-energy surfaces (Sec. III A) and discussing diabatic, electric dipole, and spin-orbit couplings between adiabatic states of CO_2^+ (Sec. III B). Next we focus on details of the nuclear dynamics leading to $\text{O}(^3P_g) + \text{CO}^+(X^2\Sigma^+)$ and $\text{O}^+(^4S_u) + \text{CO}(X^1\Sigma^+)$ fragmentation (Sec. III D). We conclude with a brief summary and outlook in Sec. IV. Unless indicated otherwise, we use atomic units (a.u.) throughout this work.

II. NUMERICAL MODEL

A. Pump step: XUV ionization

Our theoretical model addresses a common implementation of time-resolved dissociative ionization experiments, in which a femtosecond XUV pump pulse rapidly ionizes a molecule and generates a vibrationally excited molecular cation [4,12,22,24,31]. For the intensity range and wavelength we consider, the pump pulse primarily populates the $X^2\Pi_g$, $A^2\Pi_u$, and $B^2\Sigma_u^+$ states of CO_2^+ [27,37,47,48], i.e., the few lowest electronic states of the molecular cation. Assuming instantaneous single ionization of CO_2 by such an ultrashort pump pulse, an estimate for the population of specific vibronic levels of the molecular cation can be obtained in the FC approximation, i.e., for vertical electronic transitions at time $t = 0$ from the electronic and vibronic ground states of CO_2 . This is indicated by the vertical gray band in Fig. 1. The figure depicts a lineout of the lowest potential-energy surfaces for linear ($\varphi = 180^\circ$) CO_2^+ cations as a function of R_1 , with one C-O distance fixed at the equilibrium distance $R_2 = 2.24$ a.u. [Fig. 2(a)].

For the $X^2\Pi_g$, $A^2\Pi_u$, and $B^2\Sigma_u^+$ states CO_2^+ , we calculated the FC factors, given by the square of the overlap between the wave functions of the $\text{CO}_2(X^1\Sigma_g^+)$ vibronic ground state and a given CO_2^+ vibronic state. We obtained the largest FC factor, 0.86, for the $\text{CO}_2^+[B^2\Sigma_u^+(0, 0, 0)]$ state, in fair agreement with the value 0.92 measured and calculated in Ref. [37]. We found the second largest FC factor 0.82 for the $\text{CO}_2^+[X^2\Pi_g(0, 0, 0)]$ ground state. This state lies 3.537 and 4.300 eV below the lowest vibronic $\text{CO}_2^+(A^2\Pi_u)$ and $\text{CO}_2^+(B^2\Sigma_u^+)$ levels, respectively, which are populated by dipole transitions in the probe-laser pulse. For the 780-nm (1.59 eV photon energy) and 400-nm (3.10 eV) probe pulses considered in the present work, dipole excitations from the $\text{CO}_2^+[X^2\Pi_g(0, 0, 0)]$ to the $\text{CO}_2^+(A^2\Pi_u)$ or $\text{CO}_2^+(B^2\Sigma_u^+)$ state require the absorption of three photons and in general affect the population evolution in the $A^2\Pi_u$ and $B^2\Sigma_u^+$ states

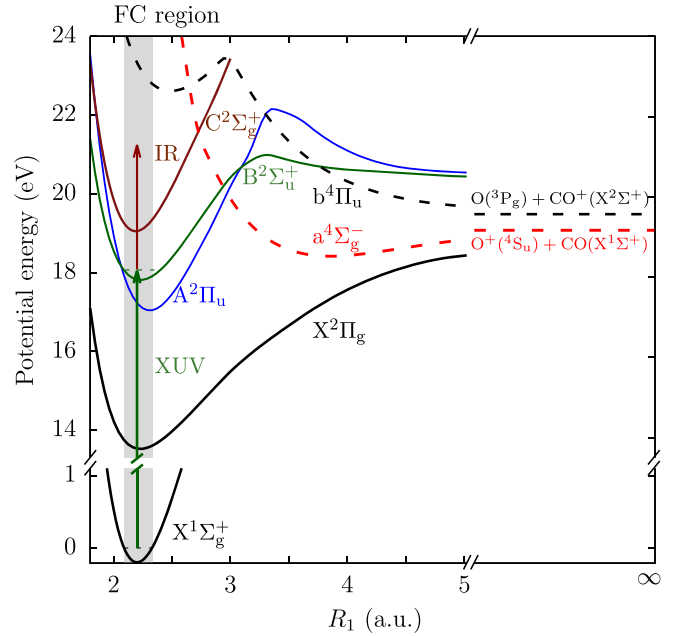


FIG. 1. Adiabatic potential energies of CO_2^+ in internuclear coordinates for $R_2 = 2.24$ a.u. and $\varphi = 180^\circ$ [cf. Fig. 2(a)]. The gray vertical band indicates the FC region, which is centered around the equilibrium configuration of $\text{CO}_2(X^1\Sigma_g^+)$. Quartet spin states are represented by dashed lines. The green arrow shows the dominant relevant FC transition to the initial $\text{CO}_2[B^2\Sigma_u^+(0, 0, 0)]$ level assumed in our propagation calculation. The threshold energies for $\text{O}^+(^4S_u) + \text{CO}(X^1\Sigma^+)$ and $\text{O}(^3P_g) + \text{CO}^+(X^2\Sigma^+)$ dissociation relative to $B^2\Sigma_u^+(0, 0, 0)$ level are 0.994 and 1.393 eV, respectively.

of interest in the present work. Furthermore, for the assumed initial alignment of the molecular cation with the laser-pulse polarization, $X^2\Pi_g \Rightarrow C^2\Sigma_g^+$ transitions are forbidden by dipole selection rules [49]. For this reason, for the dominant initial $\text{CO}_2^+[B^2\Sigma_u^+(0, 0, 0)]$ excitation in the pump step and for the probe-pulse intensity in our numerical applications, we neglect excitations from the occupied vibronic levels in the $X^2\Pi_g$ state of CO_2^+ , assuming its population to remain permanently trapped and irrelevant within the context of this work.

The FC overlap of the CO_2 ground state with the lowest vibronic level in the $\text{CO}_2^+(B^2\Sigma_u^+)$ state strongly dominates the FC factors with all other vibronic levels in the $\text{CO}_2^+(A^2\Pi_u)$ state. While the net initial population of the $\text{CO}_2^+(A^2\Pi_u)$ state is comparable to the net initial $\text{CO}_2^+(B^2\Sigma_u^+)$ state population, due to the weak coupling between these two states, in our numerical application below it merely forms a background whose effect on the fragmentation we neglect. We therefore

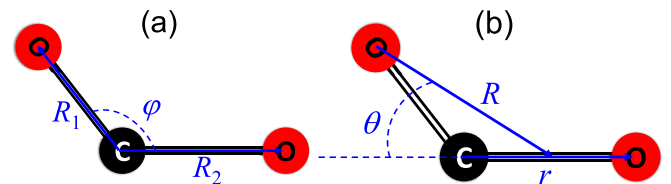


FIG. 2. (a) Internuclear and (b) Jacobi coordinates.

may assume the pump pulse to prepare the molecular cation in the $B^2\Sigma_u^+$ vibronic ground state [27,37,47].

Besides the FC factors, we note that the actual population by the pump pulse of specific cationic states depends on the electronic transition amplitudes and is more accurately reflected in the partial cross sections for single ionization of CO₂. Indeed, the partial single-ionization cross sections compiled in Ref. [50] show that, for the pump-pulse parameters in Fig. 1 of the Supplemental Material in Ref. [12] of interest here, vibronic levels in the $X^2\Pi_g$, $A^2\Pi_u$, and $B^2\Sigma_u^+$ states of CO₂⁺ receive comparable initial populations. This confirms the conclusions reached within the FC approximation.

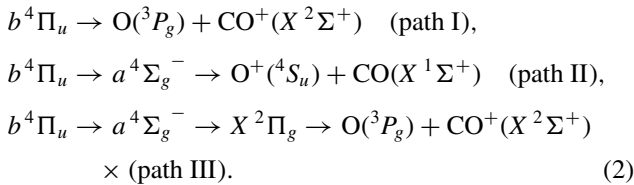
B. Probe step: IR- or VIS-induced dissociation

The probability density of the initially populated lowest vibronic level in the CO₂⁺ ($B^2\Sigma_u^+$) electronic state overlaps the conical intersection of the cationic $A^2\Pi_u$ and $B^2\Sigma_u^+$ states (cf. Fig. 1). Therefore, immediately after being populated by the pump process, the $B^2\Sigma_u^+$ state starts getting partially depleted by nonadiabatic population transfer to the $A^2\Pi_u$ state and gives rise to an oscillating nuclear wave packet in the potential well of the cationic $A^2\Pi_u$ potential-energy surface. The ensuing nuclear dynamics in CO₂⁺ is altered by the femtosecond IR or VIS probe-laser pulse, which reaches its peak intensity E_0 at a tunable delay τ after the pump step.

We model the electric field of the linearly polarized probe pulse with a Gaussian temporal profile

$$E(t) = E_0 \exp\left[-2 \ln 2 \left(\frac{t - \tau}{t_{\text{FWHM}}}\right)^2\right] \cos[\omega(t - \tau)], \quad (1)$$

where t_{FWHM} designates the full pulse width at half its intensity maximum. Exposed to the probe pulse, the CO₂⁺ molecular ion can absorb and release probe photons. Assuming the molecular cation is aligned along the polarization direction of the probe pulse, parallel electric dipole transitions are allowed between the $B^2\Sigma_u^+$ and $C^2\Sigma_g^+$ states and forbidden between the $A^2\Pi_u$ and $C^2\Sigma_g^+$ states of CO₂⁺. The delayed IR or VIS pulses destructively probe the cationic nuclear dynamics through dipole transitions to the predissociative CO₂⁺ ($C^2\Sigma_g^+$) state, subsequent spin-orbit coupling to the dissociative CO₂⁺ ($b^4\Pi_u$) state, and eventual dissociation along one of the following paths [36,38,51,52]:



The probe process thus necessitates dipole transitions in the probe-laser field and spin-changing transitions between spin-doublet and spin-quartet states. In addition, it is sensitive to nonadiabatic (non-BO) coupling at the conical intersection of the $A^2\Pi_u$ and $B^2\Sigma_u^+$ states.

In comparison to path I, path III [cf. Eq. (2)] requires two additional transitions, mediated by the spin-orbit coupling between the $a^4\Sigma_g^-$ and $X^2\Pi_g$ states and coupling of

the spin-quartet states. Due to this more convoluted coupling scheme, path III is expected to contribute very little to the $\text{O}({}^3P_g) + \text{CO}^+(X^2\Sigma^+)$ yield and will not be included in our numerical application in Sec. III.

C. Nuclear dynamics

For the initial-state preparation by the XUV pump pulse and including the influence of the delayed IR or VIS probe-laser field (1), we solve the TDSE for the evolution of the CO₂⁺ nuclear wave function out of the lowest vibronic level in the $B^2\Sigma_u^+$ state in full [three-dimensional (3D)] dimensionality. Within the subspace spanned by the relevant electronic states $A^2\Pi_u$, $B^2\Sigma_u^+$, $C^2\Sigma_g^+$, $a^4\Sigma_g^-$, and $b^4\Pi_u$ of CO₂⁺ (alternatively identified as A , B , C , a , and b , respectively), the TDSE assumes the coupled-channel representation [53–55]

$$i \frac{\partial}{\partial t} \begin{pmatrix} \psi_A \\ \psi_B \\ \psi_C \\ \psi_b \\ \psi_a \end{pmatrix} = \mathbf{H} \begin{pmatrix} \psi_A \\ \psi_B \\ \psi_C \\ \psi_b \\ \psi_a \end{pmatrix}, \quad (3)$$

with the Hamiltonian

$$\mathbf{H} = \begin{pmatrix} T + V_A & V_{AB} & \vec{E}(t)\vec{d}_{AC} & 0 & 0 \\ V_{AB} & T + V_B & \vec{E}(t)\vec{d}_{BC} & 0 & 0 \\ \vec{E}(t)\vec{d}_{AC} & \vec{E}(t)\vec{d}_{BC} & T + V_C & V_{Cb}^{SC} & 0 \\ 0 & 0 & V_{Cb}^{SC} & T + V_b & V_{ba}^{SC} \\ 0 & 0 & 0 & V_{ba}^{SC} & T + V_a \end{pmatrix}. \quad (4)$$

This representation fully accounts for symmetric stretch, bending, and antisymmetric stretch vibronic excitations of CO₂⁺ in the body frame of the molecular ion. In diabatic representation, the potential energies of the states A and B , and their diabatic coupling, are designated as V_A , V_B , and V_{AB} , respectively. In addition, V_C , V_a , V_b , V_{Cb}^{SC} , and V_{ba}^{SC} are the adiabatic potential energies of the states C , a , and b , the spin-orbit couplings of state C with state b , and the angular-momentum-changing coupling of the quartet states a and b , respectively. The probe-laser electric field $\vec{E}(t)$ of magnitude (1) is assumed to be oriented along the symmetry axis of the initially unbent molecular ion. It gives rise to parallel laser-dipole couplings \vec{d}_{AC} and \vec{d}_{BC} of states A and B with state C , respectively. We note that similar representations of the Hamiltonian matrix, referring to both adiabatic and diabatic basis states, have been successfully applied to study photoelectron spectra of SO₂ and N₂ [40,56].

We solve Eqs. (3) and (4) in Jacobi coordinates (r, R, θ) , where r is the C-O distance, R the distance between O and the center of mass of CO, and θ the angle between \vec{r} and \vec{R} [Fig. 2(b)]. In Jacobi coordinates, the nuclear kinetic-energy operator can be split as

$$T = T_1 + T_2 + T_{\text{iv}}, \quad (5)$$

$$T_1 = -\frac{1}{2\mu_1} \frac{\partial}{\partial r^2} - \frac{1}{2\mu_2} \frac{\partial}{\partial R^2}, \quad (6)$$

$$T_2 = -\frac{1}{2} \left(\frac{1}{\mu_1 r^2} + \frac{1}{\mu_2 R^2} \right) \frac{1}{\sin \theta} \frac{\partial}{\partial \theta} \left(\sin \theta \frac{\partial}{\partial \theta} \right), \quad (7)$$

$$T_{rv} = \frac{J(J+1) - 2K^2}{2\mu_2 R^2} + \frac{K^2}{2 \sin^2 \theta} \left(\frac{1}{\mu_1 r^2} + \frac{1}{\mu_2 R^2} \right), \quad (8)$$

with the reduced masses

$$\mu_1 = \frac{m_O m_C}{m_O + m_C}, \quad \mu_2 = \frac{m_O (m_C + m_O)}{m_O + m_C + m_O} \quad (9)$$

and the carbon and oxygen nuclear masses in atomic mass units (amu) $m_C = 12.0107$ amu and $m_O = 15.9994$ amu.

The rovibronic kinetic energy T_{rv} depends on the total angular-momentum quantum number of the molecule J and the quantum number K that specifies the projection of the total molecular angular momentum on the internal molecular figure axis, where $-J \leq K \leq J$. The full expression for T_{rv} includes off-diagonal terms in K . These off-diagonal Coriolis couplings tend to be small for small bend angles and low-lying bending modes [cf. [57] and Eq. (20) in [53]]. They were found numerically to be negligible in KCN and ArHCl (see [53] and references therein) and are not included in the present work. We note that the specific form of the kinetic-energy operator in Eq. (6) refers to our use in all numerical calculations of the scaled nuclear wave function $\psi(r, R, \theta) = rR\Psi(r, R, \theta)$, rather than $\Psi(r, R, \theta)$.

To numerically solve the TDSE (3), we apply the split-operator wave-function-propagation method [6,58], advancing the nuclear wave function $\psi = (\psi_A, \psi_B, \psi_C, \psi_b, \psi_a)^\dagger$ in increments of small time steps Δt ,

$$\begin{aligned} \psi(t + \Delta t) &= \exp\left(\frac{-i\Delta t(\mathbf{V} + \mathbf{T}_{rv})}{2}\right) \exp\left(\frac{-i\Delta t\mathbf{T}_2}{2}\right) \\ &\times \exp(-i\Delta t\mathbf{T}_1) \exp\left(\frac{-i\Delta t\mathbf{T}_2}{2}\right) \\ &\times \exp\left(\frac{-i\Delta t(\mathbf{V} + \mathbf{T}_{rv})}{2}\right) \psi(t) + O(\Delta t^3). \end{aligned} \quad (10)$$

Including the coherent nuclear dynamics in the five coupled electronic states of CO_2^+ in Eq. (4), the potential-energy matrix in (10) is given by

$$\mathbf{V} = \begin{pmatrix} V_A & V_{AB} & \vec{E}(t)\vec{d}_{AC} & 0 & 0 \\ V_{AB} & V_B & \vec{E}(t)\vec{d}_{BC} & 0 & 0 \\ \vec{E}(t)\vec{d}_{AC} & \vec{E}(t)\vec{d}_{BC} & V_C & V_{Cb}^{SC} & 0 \\ 0 & 0 & V_{Cb}^{SC} & V_b & V_{ba}^{SC} \\ 0 & 0 & 0 & V_{ba}^{SC} & V_a \end{pmatrix}. \quad (11)$$

We implemented the wave-function propagation (10) using a matrix decomposition for the exponentiated potential operator $\exp[-i\Delta t(\mathbf{V} + \mathbf{T}_{rv})/2]$ [58], a discrete-variable representation (DVR) based on Legendre polynomials for the kinetic-energy operator $\exp(-i\Delta t\mathbf{T}_2/2)$ [55,59,60], and a fast Fourier transformation algorithm for the kinetic-energy operator $\exp(-i\Delta t\mathbf{T}_1)$ [61,62]. For the numerical applications in Sec. III, we propagated in time steps of 3 a.u. We represented the Jacobi coordinates on a numerical grid covering

the intervals $r \in [1.5, 12]$ a.u., $R \in [2.5, R_\infty = 20]$ a.u., and $\theta \in [0^\circ, 180^\circ]$, with 448 and 640 equidistant grid points for r and R , respectively, and 180 DVR points for θ .

We note that the state designations used above for the few lowest states of CO_2^+ , rigorously regarded, lose their meaning for asymmetric ($R_1 \neq R_2$) and bent ($\theta > 0$) molecular ions, for which parity labels (g and u) and electronic angular-momentum projections (Σ and Π) are not (or not well) defined. Moreover, the twofold degeneracy of the $A^2\Pi_u$ and $b^4\Pi_u$ states of the linear CO_2^+ is lifted in the bent geometry [36,38]. In each of these two states, we neglect the state with the higher energy, with the following justifications.

By bending the molecular ion, the reduction in symmetry from $D_{\infty h}$ to C_s leads to the substitution of the unbent degenerate $A^2\Pi_u$ state by the states $A^2\Pi_u(A')$ and $A^2\Pi_u(A'')$ and replaces the nondegenerate unbent $B^2\Sigma_u^+$ by the bent $B^2\Sigma_u^+(A')$ state. For the asymmetric and bent geometry, the vibronic motion only couples the lower $A^2\Pi_u(A')$ term to the $B^2\Sigma_u^+(A')$ state of equal symmetry. This is confirmed by our numerical applications that are based on the multiconfigurational self-consistent-field (MCSCF) quantum-chemistry code GAMESS [63].

With regard to the $b^4\Pi_u$ state of the linear molecular ion, symmetry reduction leads the two states $b^4\Pi_u(^4B_1)$ and $b^4\Pi_u(^4A_1)$. The upper 4A_1 term shifts upward in energy for increasing bent angles, while the lower 4B_1 term shifts downward towards the lowest dissociation threshold [36]. The 4B_1 term is thus expected to be dynamically populated and essential for dissociation into the two lowest dissociation channels considered in this work. In contrast, the 4A_1 term is of little relevance and neglected in our calculations [36,51].

D. Fragment yields

As observables, we calculated the fragment yields in the dissociation channels I and II in Eq. (2). Referring to these channels with indices $i = \text{I}$ and II , respectively, the yields for obtaining CO^+ ($i = \text{I}$) and CO ($i = \text{II}$) fragments with vibrational quantum number v and rotational quantum number j are obtained by projecting the numerically propagated nuclear wave functions ψ_i onto asymptotic states,

$$\begin{aligned} S_i(E_k, vj, \tau) &= \frac{\mu_2}{2\pi k} \left| \int_{R_{\min}}^{R_\infty} dR e^{-ikR} \int_{r_{\min}}^{r_{\max}} dr \chi_{i,vj}(r) \right. \\ &\times \left. \int_0^\pi d\theta \sin \theta \psi_i(r, R, \theta, \tau) \phi_j(\theta) \right|^2. \end{aligned} \quad (12)$$

The asymptotic states $\phi_j(\theta) = \sqrt{(2j+1)/2} P_j(\cos \theta)$ and $\chi_{i,vj}(r)$ represent free-rotor states and rovibrational states of CO^+ or CO fragments, respectively. The plane-wave factor $\exp(-ikR)$ represents the asymptotic relative fragment motion (at $R \rightarrow \infty$) with net KER $E_k = k^2/2\mu_2$. The net KER in channel I is related to the asymptotic fragment energies E_k^O and $E_k^{\text{CO}^+}$ by $E_k = 4m_O E_k^O / \mu_2 = 4m_{\text{CO}^+} E_k^{\text{CO}^+} / \mu_2$, with an obvious interchange of the fragment charges in channel II. The ψ_i is equal to the nuclear-wave-function components in the dissociation channels, i.e., $\psi_{\text{I}} = \psi_b$ and $\psi_{\text{II}} = \psi_a$. We numerically propagated the TDSE for a sufficiently long time past the probe pulse to ensure convergence of the yields S_i .

For all numerical applications in Sec. III we set $r_{\min} = 1.5$, $r_{\max} = 12$, and $R_{\min} = 6$ a.u., after testing numerically that further extension of the ranges of r and R does not noticeably change S_i . The minimal distance R_{\min} needs to be large enough so that the overlap of the fragment nuclear wave functions can be neglected.

In the experiments we model, the internal energies E_{vj} of the CO and CO⁺ fragments are not resolved. We therefore compute the yields in channels I and II as functions of the KER E_k and pump-probe delay τ as sums over all rovibrational internal dimer excitations,

$$S_i(E_k, \tau) = \sum_{vj} S_i(E_k, vj, \tau). \quad (13)$$

The total fragment yields as a function of the time delay follow by integration,

$$S_i(\tau) = \int S_i(E_k, \tau) dE_k. \quad (14)$$

The fragment power spectrum allows the analysis of the dissociation dynamics in the frequency domain in terms of quantum beats between the vibronic nuclear-wave-packet components [28,33]. It is obtained as a function of the quantum-beat frequency f from the coherent fragment yield

$$S_i^{\text{coh}}(E_k, \tau) = S_i(E_k, \tau) - S_i^{\text{incoh}}(E_k), \quad (15)$$

as the windowed Fourier transformation

$$P_i(f, E_k) = \left| \int_{\tau_{\min}}^{\tau_{\max}} S_i^{\text{coh}}(E_k, \tau) \exp(i2\pi f\tau) H(\tau) d\tau \right|^2, \quad (16)$$

where the incoherent delay-independent term is given by

$$S_i^{\text{incoh}}(E_k) = \frac{1}{\tau_{\max} - \tau_{\min}} \int_{\tau_{\min}}^{\tau_{\max}} S_i(E_k, \tau) d\tau. \quad (17)$$

For our numerical applications in Secs. III B and III D, we use the window function

$$H(\tau) = \cos^2 \left[\frac{\pi}{\tau_{\max} - \tau_{\min}} \left(\tau - \frac{\tau_{\min} + \tau_{\max}}{2} \right) \right] \quad (18)$$

in order to suppress nonphysical transient frequencies related to the finite delay range $[\tau_{\min}, \tau_{\max}]$.

III. NUMERICAL RESULTS

In order to provide pump-probe-delay-dependent KER spectra for the dissociative ionization of CO₂, we calculated potential-energy surfaces and dipole-coupling matrix elements for CO₂⁺ by applying the MCSCF quantum-chemistry code GAMESS [63]. The fixed-nuclei molecular electronic-structure calculations were performed in the full 3D dimensionality on equidistant grids with spacing of 0.02 a.u. (R_1 and R_2) and 2° (φ) [cf. Fig. 2(a)]. We carried out the MCSCF calculations with six frozen K -shell electrons and 15 active electrons in 12 active orbitals, thereby including all atomic valence orbitals in the active space. The employed cc-pVTZ basis set, contracted to the orbitals $\{4s, 3p, 2d, 1f\}$, provides 30 atomic orbitals for each C and O atom and 188760 configuration-state functions. For these specifications, we calculated $X^2\Pi_g$, $A^2\Pi_u$, $B^2\Sigma_u^+$, $C^2\Sigma_g^+$, $a^4\Sigma_g^-$, and $b^4\Pi_u$ adiabatic electronic states. The total energy of CO₂⁺

was minimized by linearly combining these states with equal weights.

While the detailed dissociation dynamics of CO₂⁺ in the probe-laser field can only be assessed by numerically propagating the nuclear wave function, first clues to the expected nuclear motion on the coupled potential-energy surfaces are discussed in Secs. III A and III B by examining adiabatic potential-energy surfaces and their coupling. Clearly, the suggested propensities and most conclusions drawn with regard to the dissociation dynamics require confirmation by full nuclear dynamics calculations and experimental data, for which we refer to Sec. III D.

A. Adiabatic potential-energy surfaces

Figure 3 shows our numerical results for the potential-energy surfaces associated with the adiabatic electronic states $A^2\Pi_u$, $B^2\Sigma_u^+$, $C^2\Sigma_g^+$, $b^4\Pi_u$, and $a^4\Sigma_g^-$ of CO₂⁺, deemed relevant for the present investigation. The left column displays the dependence of the potential energies as a function of the C-O distances R_1 and R_2 for unbent molecular cations ($\varphi = 180^\circ$). The black dashed line in Figs. 3(a) and 3(b) retraces the conical intersection of the $A^2\Pi_u$ and $B^2\Sigma_u^+$ states. The potential well in Fig. 3(a) is more elongated along the main diagonal ($R_1 = R_2$) than the well in Fig. 3(b), suggesting that the $A^2\Pi_u$ state is more supportive of symmetric stretch modes than the $B^2\Sigma_u^+$ state. Similarly, the shape of the $B^2\Sigma_u^+$ well appears to slightly favor antisymmetric stretch modes. Nonadiabatic transitions near the conical intersection of these states are therefore expected to change the ratio of symmetric and antisymmetric vibronic modes in the nuclear-wave-packet dynamics. In contrast, the left graphs in Figs. 3(d) and 3(e) have narrow wells at unequal C-O separations that extend to infinite distances R_1 and R_2 . This is consistent with the antibonding character of the spin-quartet states that is also seen in Fig. 1. While the linear molecule in the $a^4\Sigma_g^-$ state has a shallow potential-energy well, centered at $R_1 = 2.111$ and $R_2 = 3.819$ a.u. below the lowest dissociation threshold [cf. Figs. 1 and 3(e)], the $b^4\Pi_u$ state can transiently trap population in a well at $R_1 = R_2 \approx 2.45$ a.u. [cf. Figs. 1 and 3(d)].

The right column of Fig. 3 reveals the variation of the potential energies as a function of the bend angle φ and one C-O intermolecular distance R_2 , while the other C-O distance R_1 is kept at the equilibrium distance of the CO₂ ground state, 2.24 a.u. [64]. The graphs on the right-hand side of Figs. 3(a)–3(c) show potential wells along the R_2 and φ axes that are centered at the unbent configuration ($\varphi = 180^\circ$). Along the φ axis, the well in Fig. 3(b) is comparatively narrow, suggesting that the $B^2\Sigma_u^+$ state is less susceptible to the excitation of bending modes than the $A^2\Pi_u$ and $C^2\Sigma_g^+$ states. The potential well in the $b^4\Pi_u$ state is centered at $\varphi \approx 110^\circ$ [Fig. 3(d)], suggesting that dissociation along path I in Eq. (2) proceeds via the excitation of bending modes. In contrast, as seen in Fig. 3(e), the bending well in the $a^4\Sigma_g^-$ state is aligned with the unbent molecular ion. This tends to imply that dissociation path II relies to a lesser degree on molecular bending than path I.

To assess to the accuracy of the potential-energy surfaces we obtained applying the GAMESS molecular structure code

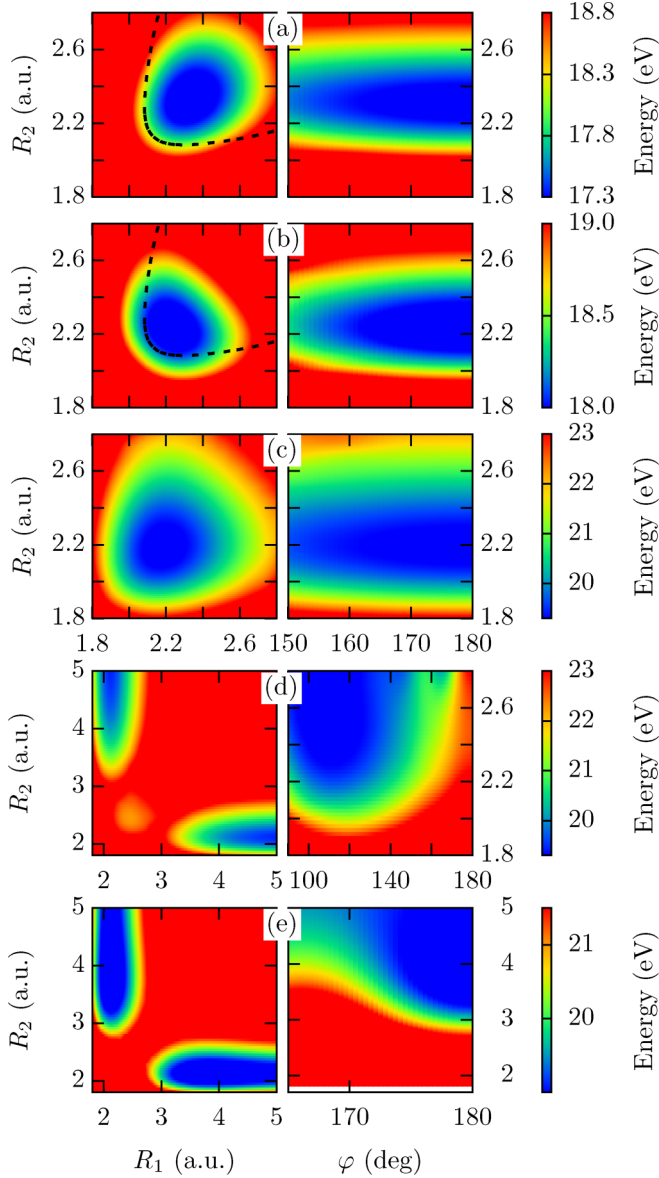


FIG. 3. Adiabatic potential-energy surfaces of the (a) $A^2\Pi_u$, (b) $B^2\Sigma_u^+$, (c) $C^2\Sigma_g^+$, (d) $b^4\Pi_u$, and (e) $a^4\Sigma_g^-$ states of CO_2^+ as functions of the C-O distances R_1 and R_2 for linear molecular ions ($\varphi = 180^\circ$) as functions of R_2 (left column) and the bend angle φ for $R_1 = 2.24$ a.u. (right column). The black dashed lines in (a) and (b) retrace the conical intersection of the $A^2\Pi_u$ and $B^2\Sigma_u^+$ states.

[63], we calculated rovibronic excitation energies in the $A^2\Pi_u$ and $B^2\Sigma_u^+$ states of CO_2^+ relative to the $X^1\Sigma_g^+(0, 0, 0)$ ground state of CO_2 . To get the vibronic energy eigenvalues, we diagonalized the Hamiltonians in the corresponding adiabatic channels using a discrete Fourier basis for the Jacobi coordinates r and R [65] and a Legendre-DVR basis for the bend angle θ [59,60]. Table I shows our numerical results for rovibronic excitations (v_s, v_b, v_a) in the $A^2\Pi_u$ and $B^2\Sigma_u^+$ electronic states in comparison with the synchrotron-based pulsed-field-ionization photoemission experiment of Liu *et al.* [37]. For symmetric stretch, bending, and antisymmetric stretch excitations with vibronic quantum numbers up to $v_s = 6$, $v_b = 7$, and $v_a = 2$, respectively, our calculated

TABLE I. Energies in eV of CO_2^+ rovibronic levels (v_s, v_b, v_a) relative to the $X^1\Sigma_g^+(0, 0, 0)$ ($J = 0$) ground state of CO_2 . Here v_s , v_b , and v_a designate quantum numbers of the symmetric stretch, bending, and antisymmetric stretch modes, respectively. The experimental energies are from Liu *et al.* [37] (column 2). Our results for adiabatic $A^2\Pi_u(J, K)$ and $B^2\Sigma_u^+(J = 0)$ states of CO_2^+ are based on MCSCF calculations with GAMESS [63] for rotational quantum numbers J and K (column 3). The differences between our calculated and the experimental energies are given in column 4. Column 5 contains the calculated energies of rovibronic levels relative to the $B^2\Sigma_u^+(0, 0, 0)$ level of CO_2^+ , which are proportional to quantum beat frequencies f .

State	Expt. (eV)	Theory (J, K) (eV)	Theory minus Expt. (meV)	hf (meV)
$A(4, 0, 0)$	17.8708	17.8740 (0,0)	3.2	-202.0
$A(0, 0, 2)$	17.9742	17.9765 (0,0)	2.3	-99.5
$A(5, 0, 0)$	18.0091	18.0089 (0,0)	-0.2	-67.1
$A(1, 0, 2)$	18.1119	18.1097 (0,0)	-2.2	33.7
$A(6, 0, 0)$	18.1480	18.1430 (0,0)	-5.0	67.0
$A(2, 0, 2)$	18.2406	18.2424 (0,0)	1.8	166.4
$A(4, 1, 0)$	17.9230	17.9299 (1,1)	6.9	-146.1
$A(5, 1, 0)$	18.0691	18.0654 (1,1)	-3.7	-10.6
$A(2, 3, 1)$		18.0773 (1,1)		1.3
$A(3, 1, 1)$		18.1127 (1,1)		36.7
$A(6, 1, 0)$	18.2006	18.2001 (1,1)	-0.5	124.1
$A(1, 3, 1)$		18.0393 (3,3)		-36.7
$A(0, 7, 1)$		18.0756 (3,3)		-0.4
$A(2, 1, 1)$		18.0809 (3,3)		4.9
$B(0, 0, 0)$	18.0760	18.0760 (0,0)	0.0	0.0
$B(0, 2, 0)$	18.2228	18.2151 (0,0)	-7.7	139.1
$B(1, 0, 0)$	18.2352	18.2325 (0,0)	-2.7	156.5
$B(0, 0, 1)$	18.3105	18.3103 (0,0)	-0.2	234.3

excitation energies agree with the experimental values within 1–8 meV.

B. Couplings between adiabatic states

Dissociative ionization into the lowest fragmentation channels I and II, distinguished in Eq. (2), requires electric dipole and spin-orbit interactions between adiabatic states and is sensitive to the diabatic coupling near the intersection of the $A^2\Pi_u$ and $B^2\Sigma_u^+$ states. These couplings are included in the Hamiltonian (4) for the nuclear dynamic in CO_2^+ and will be examined next.

1. Diabatic coupling

The Born-Oppenheimer approximation breaks down near intersections of adiabatic potential-energy surfaces, where the interaction between electronic and nuclear motion becomes important, allowing nonadiabatic processes [66]. Relevant for the present study is the intersection between the $A^2\Pi_u$ and $B^2\Sigma_u^+$ adiabatic states of CO_2^+ . This crossing is located in the Franck-Condon overlap region, indicated by the gray vertical band in Fig. 1, and therefore is accessed immediately after the initial ionization of the neutral parent molecule by the XUV pump pulse. Due to the absence of other energetically close degenerate states, the localized non-BO vibronic

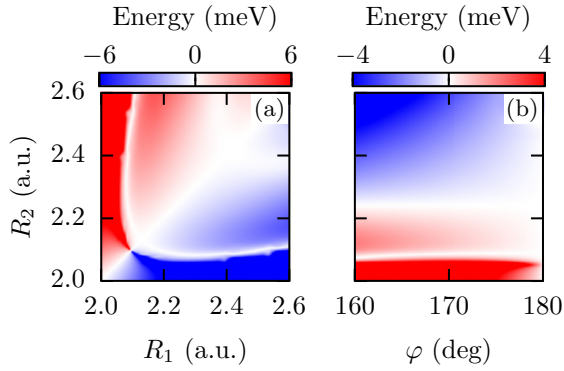


FIG. 4. Diabatic coupling V_{AB} in meV as a function of (a) the C-O distances R_1 and R_2 for the OCO angle $\varphi = 170^\circ$ and (b) R_2 and φ for $R_1 = 2.24$ a.u.

coupling can be analyzed within a two-state model, based solely on either the two adiabatic states $A^2\Pi_u$ and $B^2\Sigma_u^+$ or two corresponding diabatic states. In this adiabatic or diabatic two-state model, the nuclear potential-energy or kinetic-energy operators are diagonal, respectively. The adiabatic potential energies are given in Fig. 3. Including symmetric stretch modes and a bilinear approximation for the coupling between the bending and antisymmetric stretch modes, the crosstalk between the adiabatic $A^2\Pi_u$ and $B^2\Sigma_u^+$ states through the vibronic nuclear motion was addressed in an insightful theoretical study by Zimmermann *et al.* [67]. In the more recent experimental and theoretical investigation of Timmers *et al.* [12], these vibronic couplings and related quantum beats between rovibronic levels were identified as the cause for their measured oscillations in the CO⁺ yield during the dissociative ionization of CO₂.

We include the influence of vibronic coupling near the intersection of the $A^2\Pi_u$ and $B^2\Sigma_u^+$ adiabatic states of CO₂⁺ on the dissociation dynamics by diabatizing the potential-energy surfaces of the adiabatic $A^2\Pi_u$ and $B^2\Sigma_u^+$ states. For this purpose, we applied the MCSCF quantum-chemistry code GAMESS [63], which implements the diabatization method described by Nakamura and Truhlar [68,69]. The resulting off-diagonal diabatic coupling V_{AB} as a function of the C-O distances R_1 and R_2 for the fixed OCO bend angle $\varphi = 170^\circ$ is shown in Fig. 4(a). This graph shows that the diabatic coupling vanishes along the diagonal, where $R_1 = R_2$, and thus complies with the symmetry selection rules. These require couplings to be mediated by antisymmetric and bending vibronic modes [67]. Plotted as a function of R_2 and φ for $R_1 = 2.24$ a.u., in Fig. 4(b) V_{AB} is seen to be zero for the linear molecular ion ($\varphi = 180^\circ$) and for $R_1 = R_2 = 2.24$ a.u. The results in Fig. 4 thus satisfy the symmetry requirement of antisymmetric vibration and bending being prerequisite for diabatic coupling between the $A^2\Pi_u$ and $B^2\Sigma_u^+$ states [67].

2. Laser-dipole coupling

We calculated the dipole-coupling matrix elements in Eq. (4), d_{AC} and d_{BC} , using converged MCSCF wave functions generated by the molecular-dynamics code GAMESS [63] together with (and for the same numerical parameters as) the

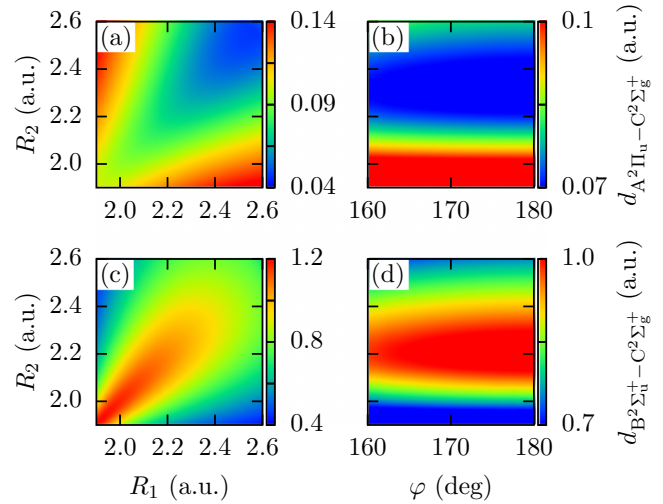


FIG. 5. Electric dipole couplings of the three lowest excited CO₂⁺ adiabatic states as functions of (a) and (c) the C-O distances R_1 and R_2 for linear molecular ions ($\varphi = 180^\circ$) and (b) and (d) R_2 and the bend angle φ for $R_1 = 2.24$ a.u. (a) and (b) Perpendicular coupling d_{AC} between $A^2\Pi_u$ and $C^2\Sigma_g^+$ states. (c) and (d) Parallel coupling d_{BC} of the $B^2\Sigma_u^+$ and $C^2\Sigma_g^+$ states.

potential-energy surfaces discussed in the preceding section. Exposed to the linearly polarized field of the IR or VIS probe laser and for the assumed parallel orientation of the probe-laser electric field and initial O-C-O molecular axis direction, the initially (at time $t = 0$) populated CO₂⁺($B^2\Sigma_u^+$) state couples to the CO₂⁺($C^2\Sigma_g^+$) state by absorbing an odd number of IR or VIS photons. The corresponding coupling matrix element d_{BC} for linear molecular cations is shown in Fig. 5(c). This coupling is most significant for comparable internuclear distances R_1 and R_2 , which suggests its propensity for exciting symmetric stretch modes in the CO₂⁺($C^2\Sigma_g^+$) state. Due to the symmetries of the coupled states Σ_u^+ and Σ_g^+ , the electric dipole coupling is strongest for the parallel orientation assumed in the present work. It is forbidden for perpendicular orientation [49]. Its broad well in the direction of the bend angle in Fig. 5(d) indicates that the strong symmetric coupling is maintained if bending modes are excited. This tends to support combined, symmetric stretch and bending, vibronic excitations during the dissociation process.

Following the ionization of the neutral CO₂ molecule in the XUV pump pulse, the CO₂⁺($B^2\Sigma_u^+$)(0, 0, 0) level feeds probability density into the CO₂⁺($A^2\Pi_u$) state by nonadiabatic coupling of the electronic and nuclear dynamics. This makes the excitation of bending modes in the $A^2\Pi_u$ state possible. Nonparallel $A^2\Pi_u \rightarrow C^2\Sigma_g^+$ excitations by the probe pulse then become dipole allowed, while being forbidden for parallel orientation [49]. The corresponding dipole-coupling matrix element in Fig. 5(a) is minimal at $R_1 = R_2$ and favors extremely unequal C-O distances R_1 and R_2 , which tends to promote the excitation of antisymmetric stretch modes. As seen in Fig. 5(b), the bending excitations may extend over a large range of bend angles φ . For very intense probe fields, this may lead to self-amplified bending of the molecular cation, as population is driven out of and back into the $A^2\Pi_u$ state.

Comparing the dipole couplings in Figs. 5(a) and 5(b) and Figs. 5(c) and 5(d), we note that in the FC region (near $R_1 = R_2 = 2.24$ a.u.) and for linear molecules, d_{BC} exceeds d_{AC} by more than an order of magnitude. For this reason, we expect $B^2\Sigma_u^+ \rightarrow C^2\Sigma_g^+$ parallel transitions to be significantly more prolific than $A^2\Pi_u \rightarrow C^2\Sigma_g^+$ perpendicular excitations in determining the fragment yields along the dissociation paths I and II in Eq. (2). As d_{BC} emphasizes smaller C-O distances, it tends to promote excitations to lower symmetric stretch modes. In contrast, the influence of d_{AC} strongly increases once antisymmetric modes have been excited. We therefore expect a small contribution of self-reinforcing vibronic heating into antisymmetric and bent modes due to $A^2\Pi_u \leftrightarrow C^2\Sigma_g^+$ coupling in the probe-laser field.

3. Spin-orbit coupling

For the XUV-pump-pulse parameters assumed in the present investigation, the fragmentation of vibronically excited CO_2^+ molecules into the two lowest dissociation channels in Eq. (2) requires spin-changing couplings between the spin-doublet state $C^2\Sigma_g^+$ and the spin-quartet state $b^4\Pi_u$, as well as angular-momentum-changing transitions between the quartet states $b^4\Pi_u$ and $a^4\Sigma_g^-$. These couplings are designated as V_{Cb}^{SC} and V_{ba}^{SC} in the Hamiltonian (4), respectively. They were calculated within a complete-active-space configuration-interaction self-consistent-field approach by Liu *et al.* [38] as functions of one of the C-O distances R_1 for linear CO_2^+ molecule, with the other C-O distance kept fixed at the equilibrium distance of the ground-state CO_2 molecule, $R_2 = 2.20$ a.u.

The spin-orbit couplings provided by Liu *et al.* [38] vary as a function of approximately $2 \leq R_1 \leq 4$ a.u., but tend to stabilize for larger R_1 at $V_{Cb}^{SC} \approx -40 \text{ cm}^{-1} = -4.96 \text{ meV}$ and $V_{ba}^{SC} \approx -30 \text{ cm}^{-1} = -3.72 \text{ meV}$. Since these spin-orbit couplings are stronger for vibronically excited (and thus stretched) $\text{CO}_2^+(C^2\Sigma_g^+)$ states, we adopted the values $V_{Cb}^{SC} = -4.96 \text{ meV}$ and $V_{ba}^{SC} = -3.72 \text{ meV}$ for our numerical applications in Sec. III C 2 and subsequent sections. In numerical tests we found that varying V_{Cb}^{SC} and V_{ba}^{SC} by $\pm 50\%$ does not change the 115-fs electron-density oscillation period found experimentally [12], but modifies, as expected, the branching ratio for dissociation along paths I and II in Eq. (2).

C. Dissociation dynamics

Throughout this work, we assume the pump process to solely populate the $B^2\Sigma_u^+(0, 0, 0)$ level of CO_2^+ at time $t = 0$ by single ionization of the $\text{CO}_2(X^1\Sigma_g^+)$ parent molecule. During the action of the pump pulse, the molecule is assumed to remain aligned with the XUV-pulse polarization direction with rotational quantum numbers $J = K = 0$.

1. External-field-free non-BO nuclear dynamics

To track the nuclear dynamics at the intersection of the $A^2\Pi_u$ and $B^2\Sigma_u^+$ states of CO_2^+ during the XUV-pump-IR-probe dissociative ionization process, we first investigate the external-field-free evolution of the nuclear CO_2^+ wave function out of the $B^2\Sigma_u^+(0, 0, 0)$ state in the absence of a probe

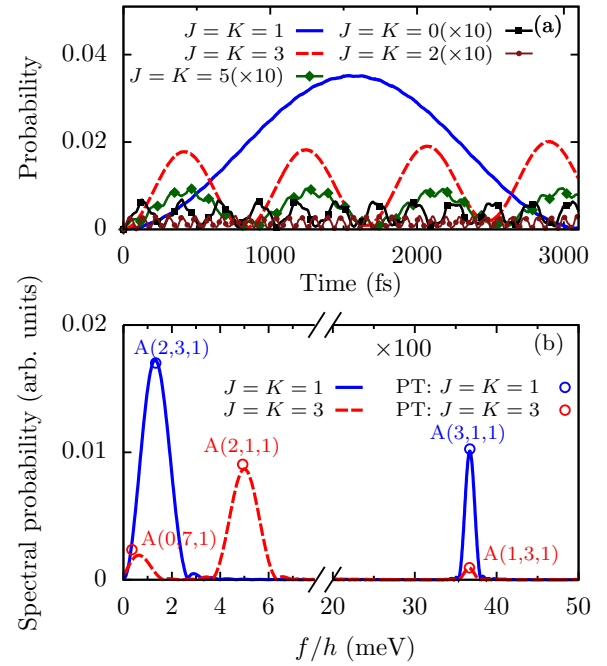


FIG. 6. (a) Probability of finding CO_2^+ in the $A^2\Pi_u$ electronic states during external-field-free nuclear-wave-packet evolution out of the initial $B^2\Sigma_u^+(0, 0, 0)$ vibronic level. (b) Fourier transform of the $A^2\Pi_u$ probability evolution. Blue and red circles show transition probabilities from the $B^2\Sigma_u^+(0, 0, 0)$ level based on perturbation theory (PT). Amplitudes for frequencies above $20 \text{ meV}/h$ are multiplied by a factor of 100.

pulse. Due to the comparatively large energetic separation of other electronic states (cf. Fig. 1), we can restrict the nuclear-wave-function evolution to the coupled $A^2\Pi_u$ and $B^2\Sigma_u^+$ states. Due to the overlap of the initial $B^2\Sigma_u^+(0, 0, 0)$ nuclear probability density with the region of strong diabatic coupling V_{AB} , nuclear probability density transfers to vibronic levels in the $\text{CO}_2^+(A^2\Pi_u)$ state. For $t > 0$, this coupling results in an evolving nuclear wave packet and oscillating vibronic population transfer in the coupled electronic two-level system.

Figure 6(a) shows the probability of finding CO_2^+ in the $A^2\Pi_u$ electronic states with different values of $J = K$ as a function of time. The probability oscillation amplitude is significantly larger for odd values of $J = K$ and for the excitation of bending modes with odd quantum numbers v_b than for even values, in agreement with Zimmermann *et al.* [67]. The dominant 3100-fs oscillation period (blue curve for $J = K = 1$) is imprinted on the entire dissociation process and agrees with the CO^+ fragment-yield oscillations measured in two independent recent pump-probe experiments [70]. A windowed Fourier transformation within the delay range $[\tau_{\min}, \tau_{\max}] = [0, 6200]$ fs of the nuclear probability-density evolution in the electronic $B^2\Sigma_u^+$ state reveals this 3100-fs oscillation as a dominant peak at a beat frequency of $f = 1.33 \text{ meV}/h$ [Fig. 6(b)]. We assign this frequency to the beating between the $B^2\Sigma_u^+(0, 0, 0)$ and $A^2\Pi_u(2, 3, 1)$ ($J = K = 1$) vibronic levels, based on their energy difference most closely matching hf (cf. Table I). This strong coupling of the $A^2\Pi_u(2, 3, 1)$ and $B^2\Sigma_u^+(0, 0, 0)$ levels was identified before by Zimmermann *et al.* [67].

Similarly, we can assign a sequence of weaker peaks in Fig. 6(b) to specific vibronic levels in the $A^2\Pi_u$ state beating against the $B^2\Sigma_u^+(0, 0, 0)$ level. The second highest peak probability is reached at $hf = 36.7$ meV, corresponding to a beat period of 113 fs. As for the dominant 3100-fs beating, this frequency transcends the molecular dissociation process. It was identified experimentally as a superimposed 115-fs oscillation in the CO⁺ fragment yield by Timmers *et al.* [12]. Based on the differences between the vibronic energies in Table I, we assign it to the interference of the $A^2\Pi_u(3, 1, 1)(J = K = 1)$ and $B^2\Sigma_u^+(0, 0, 0)$ levels (blue line), with a small contribution from the $A^2\Pi_u(1, 3, 1)(J = K = 3)$ level beating against the $B^2\Sigma_u^+(0, 0, 0)$ level (red dashed line). Within the bilinear nonadiabatic coupling model of Zimmermann *et al.* [67], the multiconfigurational time-dependent Hartree calculation of Timmers *et al.* [12] indicates quantum beats between the $A^2\Pi_u(3, 1, 1)$ and $B^2\Sigma_u^+(0, 0, 0)$ states with the frequency $f = 37.6$ meV/ h , corresponding to a period of 110 fs, in good agreement with our results.

To further validate our assignment of beating vibronic levels in Fig. 6(b), we evaluated the transition probabilities between the $B^2\Sigma_u^+(0, 0, 0)$ and $A^2\Pi_u(v_s, v_b, v_a)$ levels due to the diabatic coupling V_{AB} in first-order perturbation theory,

$$P_{A \leftrightarrow B} = 2 \left| \frac{\langle \psi_{B^2\Sigma_u^+(0,0,0)} | V_{AB} | \psi_{A^2\Pi_u(v_s, v_b, v_a)} \rangle}{E_{B^2\Sigma_u^+(0,0,0)} - E_{A^2\Pi_u(v_s, v_b, v_a)}} \right|^2. \quad (19)$$

These are shown as blue and red circles and match the ratios of the quantum-beat peak heights.

Based on the vibronic energies in Table I and consistent with the perturbative transition probabilities (19) in Fig. 6(b), we assign the beat energy 4.93 meV, corresponding to a beat period of 839 fs, to the interference of the $B^2\Sigma_u^+(0, 0, 0)$ and $A^2\Pi_u(2, 1, 1)(J = K = 3)$ levels [Fig. 6(b)]. In the same way, we relate the next weaker peak in Fig. 6(b) to the beating between the $B^2\Sigma_u^+(0, 0, 0)$ and $A^2\Pi_u(0, 7, 1)(J = K = 3)$ levels. The peak at 36.7 meV, corresponding to an oscillation period of 113 fs, overlaps the $B^2\Sigma_u^+(0, 0, 0)$ – $A^2\Pi_u(3, 1, 1)(J = K = 1)$ quantum beat we analyzed above, and is assigned to beats between the $B^2\Sigma_u^+(0, 0, 0)$ and $A^2\Pi_u(1, 3, 1)(J = K = 3)$ levels.

We note that all quantum beats identified in Fig. 6 involve $A^2\Pi_u(v_s, v_b, v_a)$ levels with $K > 0$, odd bending quantum numbers v_b , and antisymmetric stretch quantum number $v_a = 1$. This complies with the symmetry properties of the $A^2\Pi_u$ and $B^2\Sigma_u^+$ states and diabatic coupling V_{AB} [e.g., $V_{AB}(R_1, R_2, \varphi) = -V_{AB}(R_2, R_1, \varphi)$] and also with the results obtained in bilinear vibronic coupling approximation by Zimmermann *et al.* [67]. The contribution

$$\frac{K^2}{2 \sin^2 \theta} \left(\frac{1}{2\mu_1 r^2} + \frac{1}{2\mu_2 R^2} \right) \quad (20)$$

in the rovibrational kinetic-energy term T_{rv} in Eq. (8) becomes strongly repulsive near the straight configuration at $\theta = 0$ for $K > 1$, promoting these bending excitations.

2. Dissociation dynamics for a fixed pump-probe delay of 110 fs

Immediately after the sudden single ionization of the CO₂($X^1\Sigma_g^+$) parent molecule at time $t = 0$ by the pump pulse, the initial $B^2\Sigma_u^+(0, 0, 0)$ state of CO₂⁺ starts to coherently populate several vibronic levels in the electronic CO₂⁺($A^2\Pi_u$) state due to the nonadiabatic coupling enabled by its overlap with the conical intersection between the two cationic electronic states. The ensuing nuclear wave packet in the $A^2\Pi_u$ state expands the cation, since the conical intersection lies in a repulsive region of the $A^2\Pi_u$ potential-energy surface [cf. Figs. 1, 3(a), and 3(b)]. The $A^2\Pi_u$ state component of the nuclear wave packet subsequently reflects at the outer classical turning of the $A^2\Pi_u$ potential well and starts to oscillate and dephase between the inner and outer turning points of this well.

Depending on the probe-pulse delay, the nonadiabatically coupled motion in the cationic $A^2\Pi_u$ and $B^2\Sigma_u^+$ states is sooner or later subject to electric dipole transitions. For the parallel initial molecular orientation assumed in this work, the main effect of the probe laser consists in transferring population from the $B^2\Sigma_u^+$ to the predissociating $C^2\Sigma_g^+$ state of CO₂⁺, with a propensity of exciting symmetric stretch modes [cf. Fig. 5(c)]. The fragmentation process then proceeds through spin-orbit coupling to the dissociative $b^4\Pi_u$ state, following either path I or II in Eq. (2).

Our numerical solution of the nuclear TDSE, given by Eqs. (3) and (4), is based on the potential surfaces for $J = K = 0$ for the $B^2\Sigma_u^+$, $C^2\Sigma_g^+$, $a^4\Sigma_g^-$, and $b^4\Pi_u$ states. For the $A^2\Pi_u$ state, we calculate the potential-energy surface for $J = K = 1$, in order to maximize the $A^2\Pi_u$ state population and best match the experimentally observed quantum-beat frequencies, as discussed in the preceding section. We assumed a probe-laser pulse of the functional form (1) with either 780- or 400-nm central wavelength, corresponding to photon energies of 1.59 and 3.10 eV, respectively. In either case, we chose a peak intensity of 3×10^{12} W/cm² and temporal pulse width $t_{\text{FWHM}} = 45$ fs. Its carrier electric field as a function of time is shown in Fig. 7(a) for a pump-probe delay of $\tau = 110$ fs, together with the occupation probabilities for the five coupled CO₂⁺ states [Fig. 7(b)] and the expectation values in the nuclear-wave-packet components ψ_i of the molecular Jacobi coordinates $\langle r \rangle_i$, $\langle R \rangle_i$, and

$$\langle \theta \rangle_i = \frac{\int_{\pi}^0 d \cos \theta \int dR \int dr |\psi_i(r, R, \theta)|^2}{\int_{\pi}^0 d \cos \theta \int dR \int dr |\psi_i(r, R, \theta)|^2} \quad (21)$$

in Figs. 7(c), 7(d), and 7(e), respectively. Here the subscript i refers to all five (bound and dissociating) channels in Eq. (3). Due to the dominant excitation of symmetric stretch vibronic modes (cf. Sec. III C), $\langle r \rangle_i$ and $\langle R \rangle_i$ behave very similarly in Figs. 7(c) and 7(d).

In accordance with the discussion in the preceding section, our numerical results in Fig. 7(b) show an immediate small population transfer from the $B^2\Sigma_u^+$ to the $A^2\Pi_u$ state due to the diabatic coupling V_{AB} , before the onset of the pump-laser field, that lasts for about 22 fs [blue solid line in Fig. 7(b)] and expands the molecular ion [blue solid lines in Figs. 7(c) and 7(d)]. The increase of the expectation values relative to their initial values near $t = 0$ is due to the equilibrium distance

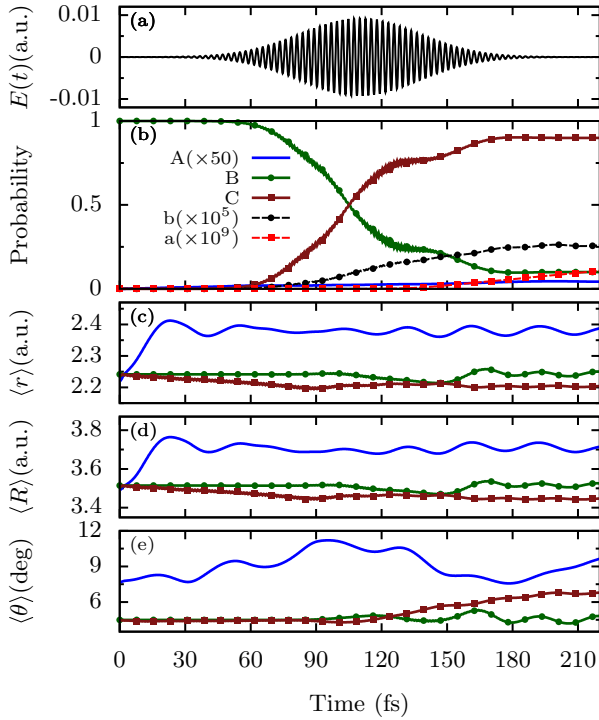


FIG. 7. CO_2^+ nuclear dynamics in a 45-fs, 3×10^{12} W/cm 2 , 780-nm probe-laser pulse. The probe-pulse center is delayed by 110 fs from the sudden initial population of the $\text{CO}_2^+[B^2\Sigma_u^+(0, 0, 0)]$ level by the XUV pump pulse at time zero. (a) Laser electric field. (b) Populations in the $A^2\Pi_u$, $B^2\Sigma_u^+$, $C^2\Sigma_g^+$, $a^4\Sigma_g^-$, and $b^4\Pi_u$ states. Expectation values (c) $\langle r \rangle_i$, (d) $\langle R \rangle_i$, and (e) $\langle \theta \rangle_i$ of the nuclear Jacobi coordinates (r, R, θ).

of the $A^2\Pi_u$ potential well being larger than the equilibrium distance of the $B^2\Sigma_u^+$ state (cf. Fig. 1). Subsequently, the nuclear-wave-packet component in the $A^2\Pi_u$ state moves to the outer turning point of the $A^2\Pi_u$ potential well, where it starts to reflect onto itself at $t \approx 22$ fs, contracting the molecule.

The expectation value of the bend angle $\langle \theta \rangle_i$ is a measure of the angular width of the nuclear probability density $|\psi_i(r, R, \theta)|^2$ [blue solid line in Fig. 7(e)]. It undergoes cycles of small-amplitude angular spreading and contraction. These cycles are nonuniform in period due to the onset of the probe-laser pulse [Fig. 7(a)] and dephasing of the nuclear wave packet [10,18]. The smaller amplitude of this oscillation after $t \approx 90$ fs is consistent with partial population back transfer from the $A^2\Pi_u$ to the $B^2\Sigma_u^+$ state, when the $A^2\Pi_u$ state broadened nuclear wave packet revisits the conical intersection. In Sec. III D 3 we will more accurately characterize these oscillations in terms of quantum beats between vibronic levels in specific electronic states of CO_2^+ .

With the onset of the pump-laser electric field at $t \approx 60$ fs, the initial $B^2\Sigma_u^+$ state population starts to quickly decline due to electric dipole transitions into the $C^2\Sigma_g^+$ state [green and brown solid lines with markers in Fig. 7(b)]. This population transfer from the $B^2\Sigma_u^+$ to the $C^2\Sigma_g^+$ state occurs over a large part of the probe-pulse temporal profile. It is fastest a few femtoseconds before the probe-pulse reaches its peak

intensity. Very rapid and barely resolved small oscillations in the $B^2\Sigma_u^+$ and $C^2\Sigma_g^+$ state populations are superimposed (femtosecond scale) Rabi flops between these two states in the probe pulse. Since the equilibrium distance of the potential well in the potential-energy surface of the $C^2\Sigma_g^+$ state is smaller than the equilibrium distance of the $B^2\Sigma_u^+$ state, electric dipole transitions into the $C^2\Sigma_g^+$ state tend to initially contract the molecular cation, leading to a decrease of the $\langle r \rangle_i$ and $\langle R \rangle_i$; $C^2\Sigma_g^+$ state expectation values during the first approximately 90 fs [brown solid lines with squares in Figs. 7(c) and 7(d)]. This contraction overcompensates for the expansion of the molecular cation promoted by nonadiabatic population transfer, due to the persistently comparatively small occupation of the $A^2\Pi_u$ state.

Continued population transfer into the predissociating $C^2\Sigma_g^+$ state causes a proportionate population increase in the $b^4\Pi_u$ state, due to the spin-orbit coupling V_{Cb}^{SC} [black dashed line with circles in Fig. 7(b)]. While the $b^4\Pi_u$ state population remains more than five orders of magnitude smaller than the $C^2\Sigma_g^+$ state population, it is required for fragmentation along paths I and II in Eq. (2). The coupling V_{ba}^{SC} between the $b^4\Pi_u$ and $a^4\Sigma_g^-$ states leads to a small delayed buildup of population in the $a^4\Sigma_g^-$ state, starting at approximately 150 fs. The $a^4\Sigma_g^-$ state population remains orders of magnitude below the $b^4\Pi_u$ state population [red dashed line with squares in Fig. 7(b)]. The branching ratio of dissociation paths I and II thus strongly favors path I, as expected in view of the additional coupling V_{ba}^{SC} in path II.

After about three quarters of the initial $B^2\Sigma_u^+(0, 0, 0)$ population is depleted at $t \approx 120$ fs, the transfer rate into the $C^2\Sigma_g^+$ state noticeably decreases, and the $B^2\Sigma_u^+$ state population eventually saturates at 9.98% of its initial value [green solid line with circles in Fig. 7(b)]. The weak $A^2\Pi_u$ population continues to slowly increase, due to ongoing diabatic coupling with the $B^2\Sigma_u^+$ state.

The angular widths $\langle \theta \rangle_{B^2\Sigma_u^+, C^2\Sigma_g^+}$ in the dominantly populated $B^2\Sigma_u^+$ and $C^2\Sigma_g^+$ states remain constant for the first approximately 90 fs, before starting to oscillate. Overall, the angular width of the $C^2\Sigma_g^+$ state slightly increases [brown solid line with squares in Fig. 7(e)]. The $\langle \theta \rangle_i$ in the dominantly populated $B^2\Sigma_u^+$ and $C^2\Sigma_g^+$ states remaining limited within a rather narrow angular range indicates a small internal-energy conversion to excited bending modes, as discussed in Sec. III B 2. The molecular cation mainly retains its linear configuration, in agreement with experimental data in Ref. [3]. We further analyze the oscillation of tens of femtoseconds in $\langle \theta \rangle_i$, $\langle r \rangle_i$, and $\langle R \rangle_i$ after approximately 120 fs in Sec. III D 3.

D. Fragment KER spectra

1. Fragment yield and $\text{CO}^{0,+}$ fragment-excitation distribution for a fixed pump-probe delay of 110 fs

Starting in the aligned $B^2\Sigma_u^+(0, 0, 0)$ state of CO_2^+ , dipole-allowed excitations to the predissociating $C^2\Sigma_g^+$ state in 780-nm (1.59 eV photon energy) or 400-nm (3.10 eV photon energy) probe pulses require the absorption of one, three, or more photons to overcome the threshold

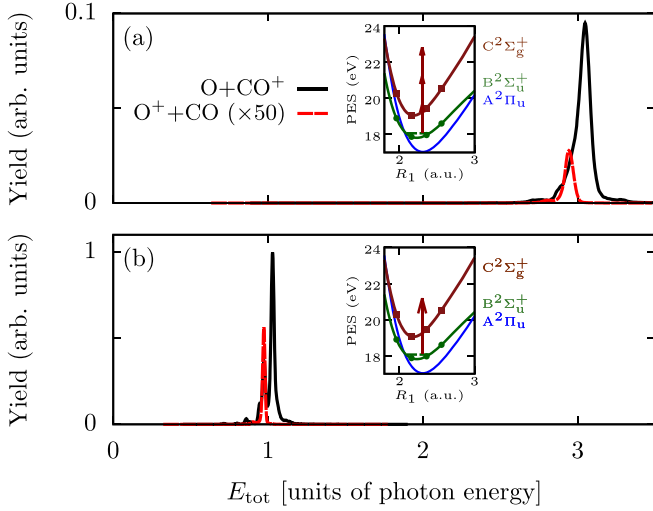


FIG. 8. Fragment yields as a function of the total energy E_{tot} relative to the $\text{CO}_2^+[B^2\Sigma_u^+(0, 0, 0)]$ ground state for 45-fs (FWHM), 3×10^{12} W/cm² peak intensity probe pulses with wavelengths of (a) 780 nm and (b) 400 nm. The pump-probe delay is 110 fs. Here E_{tot} is the sum of the fragments' KER and internal excitation energy, given in units of the respective probe-pulse photon energy. The insets illustrate the three- and one-probe-pulse-photon absorption steps during fragmentation.

energies for dissociation into the $\text{O}(^3P_g) + \text{CO}^+(X^2\Sigma^+)$ and $\text{O}^+(^4S_u) + \text{CO}(X^1\Sigma^+)$ channels of $E_{\text{diss},1} = 1.393$ and $E_{\text{diss},2} = 0.994$ eV [38], respectively.

Numerically, the number of absorbed photons can be clearly seen by plotting the fragment yields $S_i(E_k, v, j, \tau)$ in Eq. (12) as a function of the total energy $E_{\text{tot}} = E_k + E_{v,j}$, rather than the KER E_k . A fixed value of E_{tot} directly relates to the energy transferred from the pump pulse to the molecular cation and allows for variable sharing between the KER and internal rovibrational excitation energies $\{E_{v,j}\}$ of the CO or CO⁺ fragments. Accordingly, the yields for fragmentation into the $\text{O}(^3P_g) + \text{CO}^+(X^2\Sigma^+)$ and $\text{O}^+(^4S_u) + \text{CO}(X^1\Sigma^+)$ channels for a pump-probe delay of 110 fs in Fig. 8(a) show pronounced peaks corresponding to the absorption of three IR photons, while virtually no yield is calculated for one-photon excitation. While for 780-nm probe pulses dissociation by single-photon absorption surpasses the dissociation threshold $E_{\text{diss},1}$, it produces no discernible fragment yield at the peak intensity of 3×10^{12} W/cm² considered here. This is explained by the corresponding photon energy (1.59 eV) being much smaller than the excitation energy, approximately equal to 5.9 eV [37,38], for vertical transitions at the equilibrium geometry from the $\text{CO}_2^+[B^2\Sigma_u^+(0, 0, 0)]$ to the $b^4\Pi_u$ state in paths I and II of Eq. (2). Thus, only the lowest vibronic levels in the $C^2\Sigma_g^+$ state are excited, which effectively do not couple to the $b^4\Pi_u$ state.

In contrast, for 400-nm probe pulses, with identical pulse length (45 fs) and peak intensity (3×10^{12} W/cm²), the absorption of a single photon with an energy of 3.10 eV far surpasses the dissociation thresholds and excites higher vibronic levels in the $C^2\Sigma_g^+$ state that expand the molecular ion and effectively couple to the $b^4\Pi_u$ state, leading to

fragmentation. In this case, three-photon absorption practically does not contribute at the given intensity [Fig. 8(b)].

The branching ratio for dissociation into the $\text{O}(^3P_g) + \text{CO}^+(X^2\Sigma^+)$ and $\text{O}^+(^4S_u) + \text{CO}(X^1\Sigma^+)$ channels, obtained by integrating the yield in Fig. 8(a) over E_k [cf. Eq. (14)], is 275. This is in sharp contrast to a branching ratio of approximately 4 obtained experimentally in Ref. [3] for 70-fs, 800-nm, 5×10^{13} W/cm² pump pulses and 30-fs, 800-nm probe pulses with significantly higher peak intensities of approximately $(3-5) \times 10^{14}$ W/cm², for which single-photon absorption dominates. A comparably small branching ratio of 4 was calculated for 19.626-eV pump and 800-nm probe pulses in Ref. [38]. In addition, by scanning the pump-pulse photon energy between 19.0701 and 19.7560 eV, the authors found increasing branching ratios for increasing photon energy. This trend of increasing branching ratios with increasing excitation energy of the molecular ion is supported by our smaller numerical branching ratio of 198 for 400-nm probe pulses. While for 400-nm pulses we reach a total energy (relative the ground state of the CO₂) of $E_{B^2\Sigma_u^+(0,0,0)} + 3.1$ eV = 21.176 eV, for 780-nm pulses we attain a slightly higher energy of $E_{B^2\Sigma_u^+(0,0,0)} + 3 \times 1.59$ eV = 22.846 eV. We note that the spin-orbit coupling matrix elements V_{Cb}^{SC} and V_{ba}^{SC} affect the branching ratio between between the CO⁺ and O+ dissociation channels, without influencing the dissociation dynamics otherwise. In view of our approximate inclusion of V_{Cb}^{SC} and V_{ba}^{SC} (cf. Sec. III B 3 above), future refined calculations of the final spin-orbit coupling step in the dissociation dynamics are needed to accurately model this branching ratio.

As a function of the KER, the yield for fragmentation into $\text{O}(^3P_g) + \text{CO}^+(X^2\Sigma^+)$ in Fig. 9(a) displays internal fragment excitations as a sequence of peaks. For the assumed 780-nm probe-pulse wavelength, three photon excitations in the probe pulse result in KERs up to $3\omega - E_{\text{diss},i} = 3.377$ and 3.776 eV for $\text{O}(^3P_g) + \text{CO}^+(X^2\Sigma^+)$ and $\text{O}^+(^4S_u) + \text{CO}(X^1\Sigma^+)$ dissociation, respectively, for the vibrational and rotational fragment quantum numbers v and j . As expected and discussed above, the yield in the $\text{O}^+(^4S_u) + \text{CO}(X^1\Sigma^+)$ channel [Fig. 9(b)] is much smaller than for $\text{O}(^3P_g) + \text{CO}^+(X^2\Sigma^+)$ breakup. Increasing V_{ba}^{SC} by a factor of 2, we find a branching ratio that is four times smaller.

Figure 9(c) shows the same fragment yields as Figs. 9(a) and 9(b) for probe-laser pulses of identical lengths (45 fs) and peak intensity (3×10^{12} W/cm²), but with a shorter wavelength of 400 nm. At 400 nm, one-photon excitations yield KERs up to $3\omega - E_{\text{diss},i}$, equal to 1.707 and 2.106 eV for $\text{O}(^3P_g) + \text{CO}^+(X^2\Sigma^+)$ and $\text{O}^+(^4S_u) + \text{CO}(X^1\Sigma^+)$ dissociation, respectively. These maximal KERs are 1.67 eV less than for 780-nm probe pulses. Accordingly, for 400-nm pulses, less energy is available to dissipate into internal dimer-fragment excitations. The 400-nm fragment KER spectra in Fig. 9(c) therefore display less structure and fewer peaks than the 780-nm spectra in Figs. 9(a) and 9(b).

For the dominant $\text{O}(^3P_g) + \text{CO}^+(X^2\Sigma^+)$ channel, distributions of the internal rovibrational CO⁺ fragment excitations (v and j) are shown in Fig. 10 for the two fragment KERs indicated by vertical black arrows in Fig. 9(a), $E_k = 0.21$ eV [Fig. 10(a)] and 0.71 eV [Fig. 10(b)]. Overall, these distributions are characterized by energy conservation (magenta dashes in the $j - v$ plane) for the absorption of three pump-

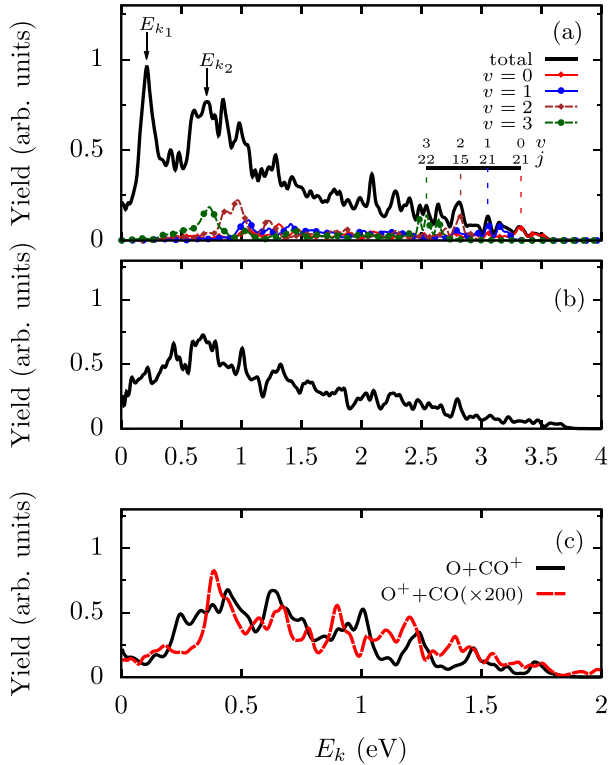


FIG. 9. Fragment yields for dissociation into (a) and (c) $O(^3P_g) + CO^+(X^2\Sigma^+)$ and (b) and (c) $O^+(^4S_u) + CO(X^1\Sigma^+)$ at a pump-probe delay of 110 fs as functions of the fragment kinetic energy E_k . The probe-pulse lengths (FWHM) and peak intensities are 45 fs and 3×10^{12} W/cm², with wavelength of (a) and (b) 780 nm and (c) 400 nm. The vibrational quantum numbers v and rotational quantum number j for selected internal CO^+ excitations are indicated on the internal axis and colored lines in (a).

pulse photons, requiring

$$|3\omega - E_{\text{diss},1} - E_k - E_{vj}| \leq \Delta, \quad (22)$$

within the spectral width $\Delta = 0.15$ eV of the 45-fs probe pulse.

As seen in Figs. 9(a) and 10(a), the CO^+ -vibrational excitation distribution is dominated by low-lying vibrational levels. Higher vibrational excitations coincide with lower KERs E_k . At $E_{k1} = 0.21$ eV, the fragment-vibrational-excitation distribution is mainly confined to $v \in [5, 10]$ [Fig. 10(a)], while at 0.71 eV it is slightly colder with $v \in [2, 8]$ [Fig. 10(b)].

2. Delay-dependent fragment KER spectra

Not resolving internal rovibrational excitations for the CO_2^+ and CO^+ fragments, we calculated pump-probe-delay- and KER-dependent fragment yields according to Eq. (13). Delay-dependent KER spectra for dissociation into the $O(^3P_g) + CO^+(X^2\Sigma^+)$ and $O^+(^4S_u) + CO(X^1\Sigma^+)$ breakup channels are shown in Figs. 11(a) and 12(a), respectively. In these graphs we subtracted the incoherent yield according to Eq. (15). As can be seen in Fig. 9, the yields have an intricate KER dependence, due to a broad spectrum of rovibrational excitations of the dimer fragments. Figures 11 and 12 show

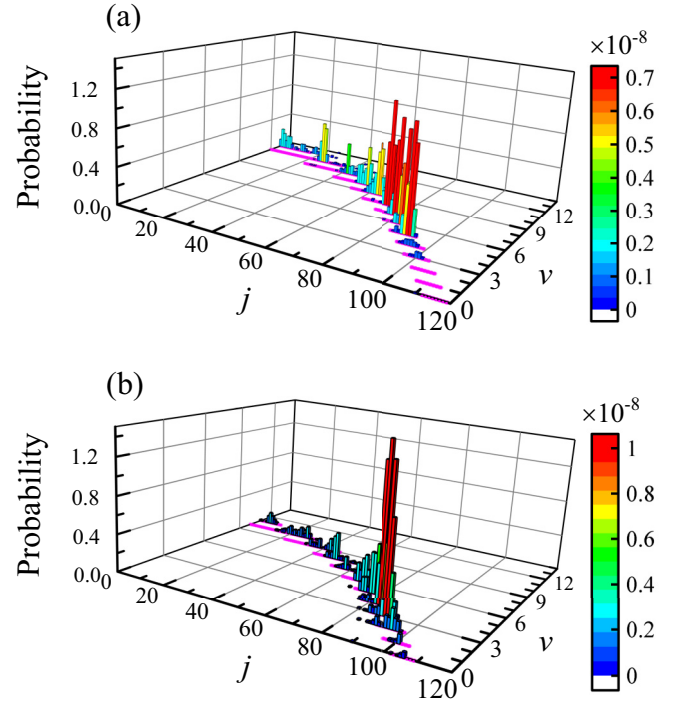


FIG. 10. Distributions of internal rovibrational CO^+ fragment excitations (v, j) for the two fragment KERs (a) $E_{k1} = 0.21$ eV and (b) $E_{k2} = 0.71$ eV, indicated by vertical black arrows in Fig. 9(a). All parameters are the same as in Fig. 9(a). The magenta dashes in the $j - v$ plane derive from energy conservation (see text for details).

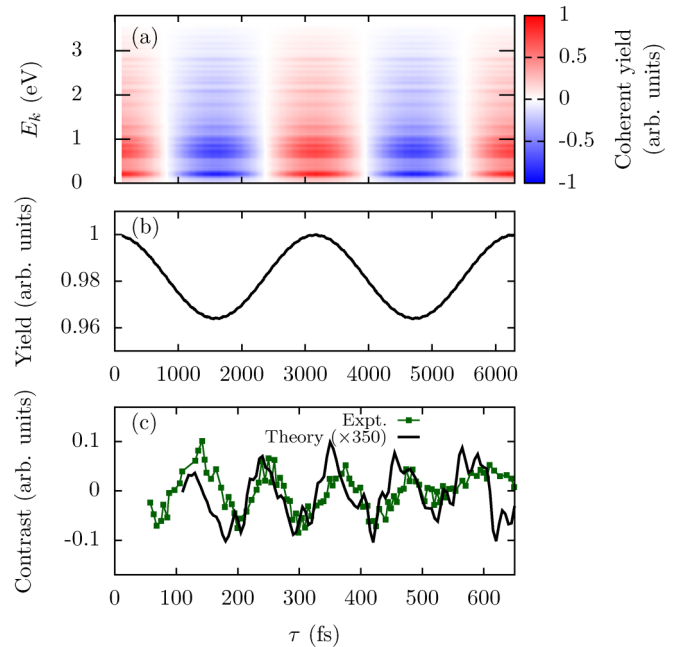


FIG. 11. (a) Coherent pump-probe-delay-dependent KER spectrum of the $O(^3P_g) + CO^+(X^2\Sigma^+)$ yield, according to Eq. (15). (b) Spectrum in (a) integrated over the KER E_k . (c) Fragment contrast in comparison with the experimental data of Timmers *et al.* [12] (green solid line with squares).

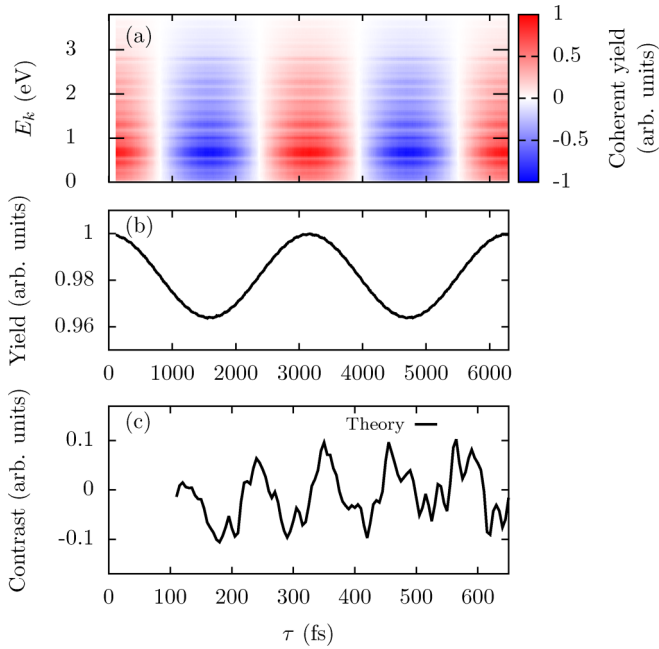


FIG. 12. Calculated spectra as in Fig. 11, but for $O^+(^4S_u) + CO(X^1\Sigma^+)$ dissociation.

that the relative yields oscillate as a function of pump-probe delay τ .

The τ -dependent relative yield variations in Figs. 11(a) and 12(a) are more clearly seen in Figs. 11(b) and 12(b), after integrating over E_k according to Eq. (14). For the $O(^3P_g) + CO^+(X^2\Sigma^+)$ channel, relative CO^+ fragment yields were measured in Ref. [12] with a superimposed, oscillating 115-fs-period pump-probe-delay dependence. This oscillation is confirmed by our theoretical model and will be analyzed below. While the calculated relative CO^+ fragment yields in Fig. 11(b) by far exceed the O^+ production yields in Fig. 12(b), the delay-dependent yield variations are very similar for the two channels and agree up to an overall factor. This confirms that details of nuclear dissociation dynamics are fully imprinted on the evolving fragment-kinetic-energy distributions by the time the two spin-quartet states get effectively coupled in the O^+ production channel [path II of Eq. (2)].

3. Quantum-beat analysis and nuclear dynamics near the $A^2\Pi_u - B^2\Sigma_u^+$ conical intersection in CO_2^+

The dynamical evolution of the nuclear wave packet can be traced to quantum beats between pairs of vibronic levels, the superposition of which constitutes the nuclear wave function [10,28]. Since the initially populated $CO_2^+[B^2\Sigma_u^+(0,0,0)]$ level instantly starts depleting at the conical interaction to give rise to a nuclear wave packet in the $A^2\Pi_u$ state (and, through “hole burning,” in the $B^2\Sigma_u^+$ state), the nuclear dynamics in CO_2^+ involves quantum beats between vibronic levels in the $B^2\Sigma_u^+$ and $A^2\Pi_u$ electronic states. These beats explain the nuclear motion leading to the delay-dependent fragment-yield oscillations in Figs. 11 and 12.

To separate and characterize these observable fragment-yield oscillations, we Fourier transform the fragment yields

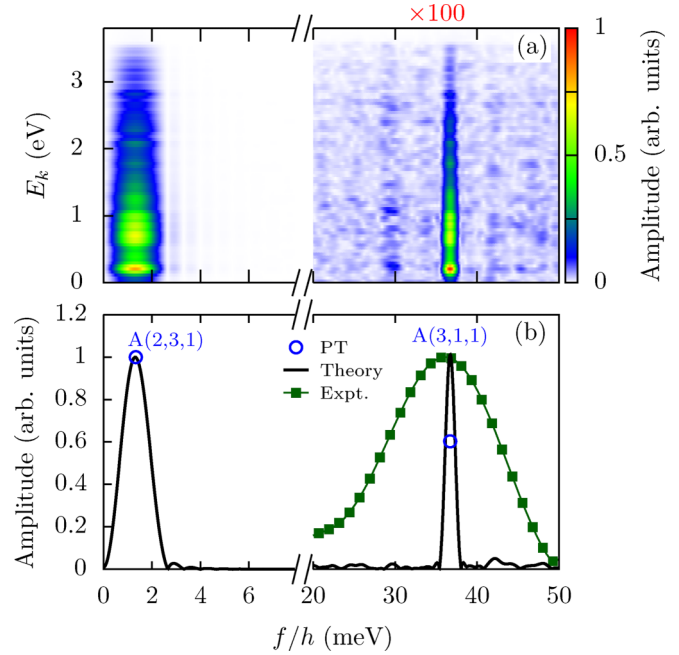


FIG. 13. (a) Power spectrum of the $O(^3P_g) + CO^+(X^2\Sigma^+)$ yield as a function of quantum-beat frequency and KER. (b) Spectrum in (a) integrated over the KER E_k (black solid line) in comparison with the power spectrum of the experimental data of Timmers *et al.* [12] in Fig. 11(b) (green solid line with squares).

in Figs. 11 and 12 according to Eq. (16), windowed within the delay range $[\tau_{\min}, \tau_{\max}] = [110, 6310]$ fs. In the quantum-beat-energy range below 50 meV, the power spectra in Figs. 13 and 14 reveal the same prominent quantum beat at $hf =$

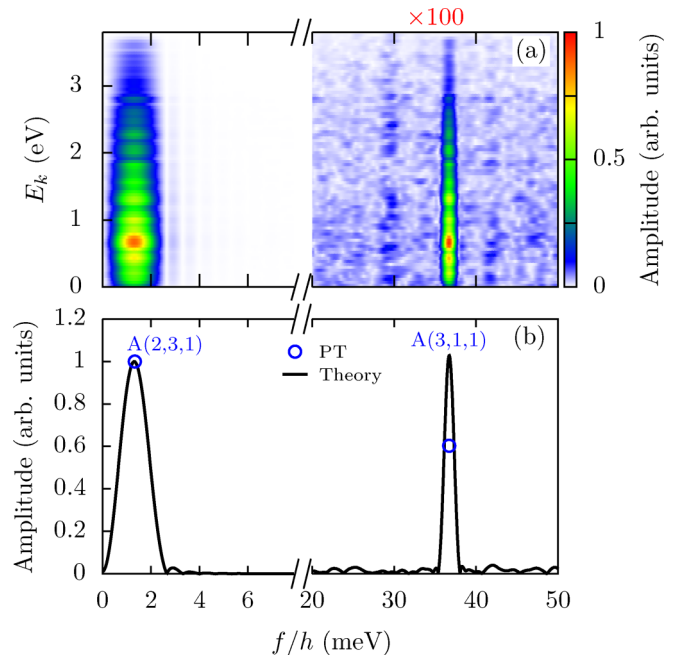


FIG. 14. (a) Power spectrum of the $O^+(^4S_u) + CO(X^1\Sigma^+)$ yield as a function of frequency and KER. (b) Graph in (a) integrated over the KER.

36.7 meV as Fig. 6 for the nuclear-wave-packet evolution under the sole influence of the diabatic coupling V_{AB} . The prominence (height) of the $A^2\Pi_u(3, 1, 1)$ peak relative to the height of the $A^2\Pi_u(2, 3, 1)$ peak is more pronounced in Figs. 13 and 14 than in Fig. 6. This is consistent with the laser dipole coupling d_{BC} favoring the less bent and more symmetric $A^2\Pi_u(3, 1, 1)$ level over the $A^2\Pi_u(2, 3, 1)$ level. Nevertheless, the subsequent pump-laser-dipole and spin-orbit couplings do not significantly affect the beating between $A^2\Pi_u$ and $B^2\Sigma_u^+(0, 0, 0)$ levels during the early, pre-pump-pulse nuclear dissociation dynamics. This applies in particular to the experimentally confirmed beat periods of approximately 3 ps ($hf = 1.364$ meV) [70] and 115 fs ($hf = 35.73$ meV) [12].

We tentatively assign the oscillations in the $B^2\Sigma_u^+$ state expectation values $\langle r \rangle_i$, $\langle R \rangle_i$, and $\langle \theta \rangle_i$ in Figs. 7(c)–7(e), starting at approximately 120 fs, to $B^2\Sigma_u^+(0, 0, 0)$ – $B^2\Sigma_u^+(0, 2, 0)$ and $B^2\Sigma_u^+(0, 0, 0)$ – $B^2\Sigma_u^+(1, 0, 0)$ quantum beats in CO_2^+ . The $B^2\Sigma_u^+(0, 2, 0)$ and $B^2\Sigma_u^+(1, 0, 0)$ levels are populated by Raman transitions in the probe pulse. Our assignment is based on the energy gap between beating vibronic levels in Table I. These are 139.1 and 156.5 meV, corresponding to oscillation periods of 30 and 26 fs, respectively. Further evidence for this assignment is provided by our nuclear dynamics calculation predicting dominant contributions during the interaction with the probe pulse by the $B^2\Sigma_u^+(0, 0, 0)$, $B^2\Sigma_u^+(0, 2, 0)$, and $B^2\Sigma_u^+(1, 0, 0)$ levels in the $B^2\Sigma_u^+$ state nuclear-wave-packet component ψ_B in Eq. (3).

IV. SUMMARY AND OUTLOOK

For single ionization of CO_2 by intense ultrashort pump pulses with central photon energies that just open the two lowest dissociation thresholds of CO_2^+ , we numerically modeled the nuclear dissociation dynamics of the pump-pulse excited molecular cation, subject to its exposure to delayed ultrashort probe pulses with a wavelength of 780 or 400 nm. Our model represents the coherent nuclear motion in the cation on the $A^2\Pi_u$, $B^2\Sigma_u^+$, $C^2\Sigma_g^+$, $a^4\Sigma_g^-$, and $b^4\Pi_u$

potential-energy surfaces of CO_2^+ in full (3D) dimensionality. It provides pump-probe-delay-dependent fragment KER spectra and allows the characterization of the nuclear-wave-packet dynamics in terms of quantum beats between specific stationary vibronic levels in different CO_2^+ electronic states. In particular, it identifies main contributions to the nuclear motion from the rovibronic levels in the $A^2\Pi_u$ and $B^2\Sigma_u^+$ adiabatic states as quantum beats. These confirm measured valence-hole oscillation periods of 115 fs [12] and approximately 3 ps [70].

The nuclear dissociation dynamics we scrutinized here in CO_2^+ requires diabatic, laser-dipole, and spin-changing interactions in order to release CO^+ and O^+ fragments into the two open dissociation channels $\text{O}(^3P_g) + \text{CO}^+(X^2\Sigma^+)$ and $\text{O}^+(^4S_u) + \text{CO}(X^1\Sigma^+)$, respectively. The physically rich and intricate combination of these interactions was shown in the present work and in Ref. [12] to reveal aspects of the significant nonadiabatic coupling between nuclear and electronic degrees of freedom at the conical intersection of the $A^2\Pi_u$ and $B^2\Sigma_u^+$ states of CO_2^+ that warrant further investigation. We plan to extend the present model by removing its restriction to initially linear molecules that are aligned with the linear pump- and probe-pulse-polarization direction. Allowing for arbitrary molecular orientation entails in particular different dipole-selection rules and alters the population transfer between relevant states in the molecular cation. This is expected to affect the coherent nuclear dynamics and therefore experimentally observable KER spectra and dominant quantum-beat oscillation periods.

ACKNOWLEDGMENTS

This work was primarily supported by the Chemical Sciences, Geosciences, and Biosciences Division, Office of Basic Energy Sciences, Office of Science, U.S. Department of Energy under Award No. DEFG02-86ER13491 (Strong-field-driven dynamics of molecules). For part of the code development and computational hardware, U.T. acknowledges partial support by NSF Grant No. PHY 2110633 (Methods development for controlling the electronic dynamics in matter). We acknowledge access to the BE Research Cluster at Kansas State University.

-
- [1] D. Polli, P. Altoè, O. Weingart, K. M. Spillane, C. Manzoni, D. Brida, G. Tomasello, G. Orlandi, P. Kukura, R. A. Mathies, M. Garavelli, and G. Cerullo, Conical intersection dynamics of the primary photoisomerization event in vision, *Nature (London)* **467**, 440 (2010).
- [2] P. M. Abanador and U. Thumm, Characterization of light-induced potentials in the strong-field dissociation of O_2^+ , *Phys. Rev. A* **102**, 053114 (2020).
- [3] M. Oppermann, S. J. Weber, F. Morales, M. Richter, S. Patchkovskii, A. Csehi, A. Vibók, M. Ivanov, O. Smirnova, and J. P. Marangos, Control and identification of strong field dissociative channels in CO_2^+ via molecular alignment, *J. Phys. B: At. Mol. Opt. Phys.* **47**, 124025 (2014).
- [4] M. Rebholz, T. Ding, L. Aufleger, M. Hartmann, K. Meyer, V. Stoob, A. Magunia, D. Wachs, P. Birk, Y. Mi *et al.*, XUV-initiated dissociation dynamics of molecular oxygen (O_2), *J. Phys. Chem. A* **125**, 10138 (2021).
- [5] B. Feuerstein and U. Thumm, Mapping of coherent and decohering nuclear wave-packet dynamics in D_2^+ with ultrashort laser pulses, *Phys. Rev. A* **67**, 063408 (2003).
- [6] B. Feuerstein and U. Thumm, Fragmentation of H_2^+ in strong 800-nm laser pulses: Initial-vibrational-state dependence, *Phys. Rev. A* **67**, 043405 (2003).
- [7] I. A. Bocharova, A. S. Alnaser, U. Thumm, T. Niederhausen, D. Ray, C. L. Cocke, and I. V. Litvinyuk, Time-resolved Coulomb-explosion imaging of nuclear wave-packet dynamics induced in diatomic molecules by intense few-cycle laser pulses, *Phys. Rev. A* **83**, 013417 (2011).
- [8] R. Boll *et al.*, X-ray multiphoton-induced coulomb explosion images complex single molecules, *Nat. Phys.* **18**, 423 (2022).

- [9] L. J. Frasinski, J. H. Posthumus, J. Plumridge, K. Codling, P. F. Taday, and A. J. Langley, Manipulation of bond hardening in H₂⁺ by chirping of intense femtosecond laser pulses, *Phys. Rev. Lett.* **83**, 3625 (1999).
- [10] M. Magrakvelidze, A. Kramer, K. Bartschat, and U. Thumm, Complementary imaging of the nuclear dynamics in laser-excited diatomic molecular ions in the time and frequency domains, *J. Phys. B: At. Mol. Opt. Phys.* **47**, 124003 (2014).
- [11] P. M. Abanador, T. Pauly, and U. Thumm, Molecular bond stabilization in the strong-field dissociation of O₂⁺, *Phys. Rev. A* **101**, 043410 (2020).
- [12] H. Timmers, Z. Li, N. Shivaram, R. Santra, O. Vendrell, and A. Sandhu, Coherent electron hole dynamics near a conical intersection, *Phys. Rev. Lett.* **113**, 113003 (2014).
- [13] M. Zhao and P. Chen, Exploring plasmonic photocatalysis via single-molecule reaction imaging, *Nano Lett.* **20**, 2939 (2020).
- [14] T. Niederhausen and U. Thumm, Controlled vibrational quenching of nuclear wave packets in D₂⁺, *Phys. Rev. A* **77**, 013407 (2008).
- [15] M. Shapiro and P. Brumer, in *Advances in Atomic, Molecular, and Optical Physics*, edited by B. Bederson and H. Walther (Academic, New York, 2000), Vol. 42, pp. 287–345.
- [16] J. M. Rondinelli and E. Kioupakis, Predicting and designing optical properties of inorganic materials, *Annu. Rev. Mater. Res.* **45**, 491 (2015).
- [17] A. S. Alnaser, B. Ulrich, X. M. Tong, I. V. Litvinyuk, C. M. Maharjan, P. Ranitovic, T. Osipov, R. Ali, S. Ghimire, Z. Chang, C. D. Lin, and C. L. Cocke, Simultaneous real-time tracking of wave packets evolving on two different potential curves in H₂⁺ and D₂⁺, *Phys. Rev. A* **72**, 030702(R) (2005).
- [18] B. Feuerstein, T. Ergler, A. Rudenko, K. Zrost, C. D. Schröter, R. Moshhammer, J. Ullrich, T. Niederhausen, and U. Thumm, Complete characterization of molecular dynamics in ultrashort laser fields, *Phys. Rev. Lett.* **99**, 153002 (2007).
- [19] B. Fischer, M. Kremer, T. Pfeifer, B. Feuerstein, V. Sharma, U. Thumm, C. D. Schröter, R. Moshhammer, and J. Ullrich, Steering the electron in H₂⁺ by nuclear wave packet dynamics, *Phys. Rev. Lett.* **105**, 223001 (2010).
- [20] G. Sansone, F. Kelkensberg, J. F. Pérez-Torres, F. Morales, M. F. Kling, W. Siu, O. Ghafur, P. Johnsson, M. Swoboda, E. Benedetti *et al.*, Electron localization following attosecond molecular photoionization, *Nature (London)* **465**, 763 (2010).
- [21] S. De, M. Magrakvelidze, I. A. Bocharova, D. Ray, W. Cao, I. Znakovskaya, H. Li, Z. Wang, G. Laurent, U. Thumm, M. F. Kling, I. V. Litvinyuk, I. Ben-Itzhak, and C. L. Cocke, Following dynamic nuclear wave packets in N₂, O₂, and CO with few-cycle infrared pulses, *Phys. Rev. A* **84**, 043410 (2011).
- [22] M. Magrakvelidze, O. Herrwerth, Y. H. Jiang, A. Rudenko, M. Kurka, L. Foucar, K. U. Kühnel, M. Kübel, N. G. Johnson, C. D. Schröter *et al.*, Tracing nuclear-wave-packet dynamics in singly and doubly charged states of N₂ and O₂ with XUV-pump-XUV-probe experiments, *Phys. Rev. A* **86**, 013415 (2012).
- [23] J. Wu, M. Magrakvelidze, A. Vredenburg, L. P. H. Schmidt, T. Jahnke, A. Czasch, R. Dörner, and U. Thumm, Steering the nuclear motion in singly ionized argon dimers with mutually detuned laser pulses, *Phys. Rev. Lett.* **110**, 033005 (2013).
- [24] P. Cörlin, A. Fischer, M. Schönwald, A. Sperl, T. Mizuno, U. Thumm, T. Pfeifer, and R. Moshhammer, Probing calculated O₂⁺ potential-energy curves with an XUV-IR pump-probe experiment, *Phys. Rev. A* **91**, 043415 (2015).
- [25] M. Kübel, M. Spanner, Z. Dube, A. Y. Naumov, S. Chelkowski, A. D. Bandrauk, M. J. J. Vrakking, P. B. Corkum, D. M. Villeneuve, and A. Staudte, Probing multiphoton light-induced molecular potentials, *Nat. Commun.* **11**, 2596 (2020).
- [26] Y. Malakar, F. Wilhelm, D. Trabert, K. R. P., X. Li, W. L. Pearson, W. Cao, B. Kaderiya, I. Ben-Itzhak, and A. Rudenko, State-selective dissociation dynamics of an oxygen molecular ion studied with single-harmonic pump and infrared-probe pulses, *Phys. Rev. A* **98**, 013418 (2018).
- [27] D. W. Turner and D. P. May, Franck-Condon factors in ionization: Experimental measurement using molecular photoelectron spectroscopy. II, *J. Chem. Phys.* **46**, 1156 (1967).
- [28] U. Thumm, T. Niederhausen, and B. Feuerstein, Time-series analysis of vibrational nuclear wave-packet dynamics in D₂⁺, *Phys. Rev. A* **77**, 063401 (2008).
- [29] T. Ergler, A. Rudenko, B. Feuerstein, K. Zrost, C. D. Schröter, R. Moshhammer, and J. Ullrich, Spatiotemporal imaging of ultrafast molecular motion: Collapse and revival of the D₂⁺ nuclear wave packet, *Phys. Rev. Lett.* **97**, 193001 (2006).
- [30] F. Anis and B. D. Esry, Role of nuclear rotation in dissociation of H₂⁺ in a short laser pulse, *Phys. Rev. A* **77**, 033416 (2008).
- [31] F. Kelkensberg, C. Lefebvre, W. Siu, O. Ghafur, T. T. Nguyen-Dang, O. Atabek, A. Keller, V. Serov, P. Johnsson *et al.*, Molecular dissociative ionization and wave-packet dynamics studied using two-color XUV and IR pump-probe spectroscopy, *Phys. Rev. Lett.* **103**, 123005 (2009).
- [32] W. Cao, G. Laurent, I. Ben-Itzhak, and C. L. Cocke, Identification of a previously unobserved dissociative ionization pathway in time-resolved photospectroscopy of the deuterium molecule, *Phys. Rev. Lett.* **114**, 113001 (2015).
- [33] M. Magrakvelidze, C. M. Aikens, and U. Thumm, Dissociation dynamics of diatomic molecules in intense laser fields: A scheme for the selection of relevant adiabatic potential curves, *Phys. Rev. A* **86**, 023402 (2012).
- [34] M. Magrakvelidze and U. Thumm, Dissociation dynamics of noble-gas dimers in intense two-color IR laser fields, *Phys. Rev. A* **88**, 013413 (2013).
- [35] N. Saito, H. Sannohe, N. Ishii, T. Kanai, N. Kosugi, Y. Wu, A. Chew, S. Han, Z. Chang, and J. Itatani, Real-time observation of electronic, vibrational, and rotational dynamics in nitric oxide with attosecond soft x-ray pulses at 400 eV, *Optica* **6**, 1542 (2019).
- [36] M. T. Praet, J. C. Lorquet, and G. Rašev, Unimolecular reaction paths of electronically excited species. IV. The C²Σ_g⁺ state of CO₂⁺, *J. Chem. Phys.* **77**, 4611 (1982).
- [37] J. Liu, M. Hochlaf, and C. Y. Ng, Pulsed field ionization-photoelectron bands for CO₂⁺ (A²Π_u and B²Σ_u⁺) in the energy range of 17.2–19.0 eV: An experimental and theoretical study, *J. Chem. Phys.* **113**, 7988 (2000).
- [38] J. Liu, W. Chen, M. Hochlaf, X. Qian, C. Chang, and C. Y. Ng, Unimolecular decay pathways of state-selected CO₂⁺ in the internal energy range of 5.2–6.2 eV: An experimental and theoretical study, *J. Chem. Phys.* **118**, 149 (2003).
- [39] I. Wilkinson, A. E. Boguslavskiy, J. Mikosch, J. B. Bertrand, H. J. Wörner, D. M. Villeneuve, M. Spanner, S. Patchkovskii, and A. Stolow, Excited state dynamics in SO₂. I. Bound state relaxation studied by time-resolved photoelectron-photoion coincidence spectroscopy, *J. Chem. Phys.* **140**, 204301 (2014).

- [40] C. Lévêque, H. Köppel, and R. Taieb, Excited state dynamics in SO_2 . III. An *ab initio* quantum study of single- and multi-photon ionization, *J. Chem. Phys.* **140**, 204303 (2014).
- [41] A. Rudenko, V. Makhija, A. Vajdi, T. Ergler, M. Schürholz, R. K. Kushawaha, J. Ullrich, R. Moshhammer, and V. Kumarappan, Strong-field-induced wave packet dynamics in carbon dioxide molecule, *Faraday Discuss.* **194**, 463 (2016).
- [42] S. Erattupuzha, S. Larimian, A. Baltuška, X. Xie, and M. Kitzler, Two-pulse control over double ionization pathways in CO_2 , *J. Chem. Phys.* **144**, 024306 (2016).
- [43] S. Zhao, B. Jochim, P. Feizollah, J. Rajput, F. Ziaee, K. R. P., B. Kaderiya, K. Borne, Y. Malakar, B. Berry *et al.*, Strong-field-induced bond rearrangement in triatomic molecules, *Phys. Rev. A* **99**, 053412 (2019).
- [44] K. Lin, X. Hu, S. Pan, F. Chen, Q. Ji, W. Zhang, H. Li, J. Qiang, F. Sun, X. Gong, H. Li, P. Lu, J. Wang, Y. Wu, and J. Wu, Femtosecond resolving photodissociation dynamics of the SO_2 molecule, *J. Phys. Chem. Lett.* **11**, 3129 (2020).
- [45] E. T. Karamatskos, S. Yarlagadda, S. Patchkovskii, M. J. J. Vrakking, R. Welsch, J. Küpper, and A. Rouzée, Time-resolving the UV-initiated photodissociation dynamics of OCS, *Faraday Discuss.* **228**, 413 (2021).
- [46] T. Severt, Z. L. Streeter, W. Iskandar, K. A. Larsen, A. Gatton, D. Trabert, B. Jochim, B. Griffin, E. G. Champenois, M. M. Brister *et al.*, Step-by-step state-selective tracking of fragmentation dynamics of water dications by momentum imaging, *Nat. Commun.* **13**, 5146 (2022).
- [47] L.-S. Wang, J. E. Reutt, Y. T. Lee, and D. A. Shirley, High resolution UV photoelectron spectroscopy of CO_2^+ , COS^+ and CS_2^+ using supersonic molecular beams, *J. Electron Spectrosc. Relat. Phenom.* **47**, 167 (1988).
- [48] P. Baltzer, F. T. Chau, J. H. D. Eland, L. Karlsson, M. Lundqvist, J. Rostas, K. Y. Tam, H. Veenhuizen, and B. Wannberg, A study of the vibronic structure in the HeI excited photoelectron spectrum of CO_2 involving the $X^2\Pi_g$ and $A^2\Pi_u$ ionic states, *J. Chem. Phys.* **104**, 8922 (1996).
- [49] H. Lefebvre-Brion and R. W. Field, *The Spectra and Dynamics of Diatomic Molecules* (Academic, San Diego, 2004), pp. 347–467.
- [50] J. Berkowitz, *Atomic and Molecular Photoabsorption: Absolute Partial Cross Sections* (Academic, New York, 2015), p. 260.
- [51] Q. Meng, M.-B. Huang, and H.-B. Chang, Theoretical study on the predissociation mechanism of $\text{CO}_2^+(\text{C}^2\Sigma_g^+)$, *J. Phys. Chem. A* **113**, 12825 (2009).
- [52] M. Yang, L. Zhang, L. Lai, D. Zhou, J. Wang, and Q. Sun, Study on the $[1 + 1']$ photodissociation spectra of CO_2^+ via $\text{C}^2\Sigma_g^+ \leftarrow \text{B}^2\Sigma_u^+/\text{A}^2\Pi_{u,1/2} \leftarrow \text{X}^2\Pi_{g,1/2}$ transitions, *Chem. Phys. Lett.* **480**, 41 (2009).
- [53] J. Tennyson and B. T. Sutcliffe, The *ab initio* calculation of the vibrational-rotational spectrum of triatomic systems in the close-coupling approach, with KCN and H_2Ne as examples, *J. Chem. Phys.* **77**, 4061 (1982).
- [54] Z. Bačić and J. C. Light, Accurate localized and delocalized vibrational states of HCN/HNC, *J. Chem. Phys.* **86**, 3065 (1987).
- [55] H. Guo, Three-dimensional photodissociation dynamics of methyl iodide, *J. Chem. Phys.* **96**, 6629 (1992).
- [56] P. Zhang, V.-H. Hoang, C. Wang, T. T. Luu, V. Svoboda, A.-T. Le, and H. J. Wörner, Effects of autoionizing resonances on wave-packet dynamics studied by time-resolved photoelectron spectroscopy, *Phys. Rev. Lett.* **130**, 153201 (2023).
- [57] B. T. Sutcliffe and J. Tennyson, A general treatment of vibration-rotation coordinates for triatomic molecules, *Int. J. Quantum Chem.* **39**, 183 (1991).
- [58] A. D. Bandrauk and H. Shen, Exponential split operator methods for solving coupled time-dependent Schrödinger equations, *J. Chem. Phys.* **99**, 1185 (1993).
- [59] J. Lill, G. Parker, and J. Light, Discrete variable representations and sudden models in quantum scattering theory, *Chem. Phys. Lett.* **89**, 483 (1982).
- [60] R. W. Heather and J. C. Light, Discrete variable theory of triatomic photodissociation, *J. Chem. Phys.* **79**, 147 (1983).
- [61] M. Feit, J. Fleck, and A. Steiger, Solution of the Schrödinger equation by a spectral method, *J. Comput. Phys.* **47**, 412 (1982).
- [62] M. Frigo and S. Johnson, The design and implementation of FFTW3, *Proc. IEEE* **93**, 216 (2005).
- [63] G. M. J. Barca *et al.*, Recent developments in the general atomic and molecular electronic structure system, *J. Chem. Phys.* **152**, 154102 (2020).
- [64] G. Herzberg, *Molecular Spectra and Molecular Structure* (Van Nostrand Reinhold, New York, 1966), Vol. III.
- [65] D. T. Colbert and W. H. Miller, A novel discrete variable representation for quantum mechanical reactive scattering via the S -matrix Kohn method, *J. Chem. Phys.* **96**, 1982 (1992).
- [66] G. A. Worth and L. S. Cederbaum, Beyond Born-Oppenheimer: Molecular dynamics through a conical intersection, *Annu. Rev. Phys. Chem.* **55**, 127 (2004).
- [67] T. Zimmermann, H. Köppel, and L. S. Cederbaum, On the bilinear vibronic coupling mechanism, *J. Chem. Phys.* **83**, 4697 (1985).
- [68] H. Nakamura and D. G. Truhlar, The direct calculation of diabatic states based on configurational uniformity, *J. Chem. Phys.* **115**, 10353 (2001).
- [69] H. Nakamura and D. G. Truhlar, Direct diabaticization of electronic states by the fourfold way. II. Dynamical correlation and rearrangement processes, *J. Chem. Phys.* **117**, 5576 (2002).
- [70] A. Rudenko and A. Sandhu (private communications).